Journal Pre-proofs

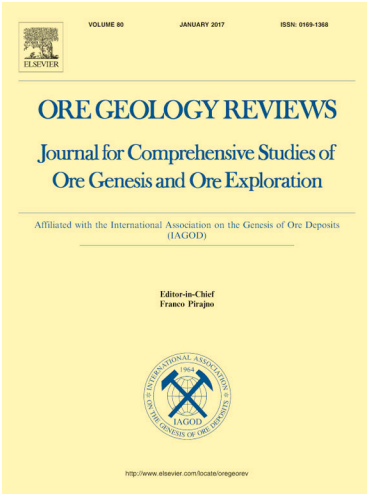

The La Lucette Sb-Au-(W) vein-deposit (Armorican Massif, France): new time and genetic constraints to decipher the 310-295 Ma Sb-Au metallogenic peak in the Variscan Belt

Florent Cheval-Garabédian, Eric Marcoux, Hugues Raimbourg, Michel Faure

PII: S0169-1368(23)00444-4
DOI: https://doi.org/10.1016/j.oregeorev.2023.105728
Reference: OREGEO 105728

To appear in: *Ore Geology Reviews*

Received Date: 11 December 2022
Revised Date: 8 October 2023
Accepted Date: 11 October 2023

Please cite this article as: F. Cheval-Garabédian, E. Marcoux, H. Raimbourg, M. Faure, The La Lucette Sb-Au-(W) vein-deposit (Armorican Massif, France): new time and genetic constraints to decipher the 310-295 Ma Sb-Au metallogenic peak in the Variscan Belt, *Ore Geology Reviews* (2023), doi: https://doi.org/10.1016/j.oregeorev.2023.105728

The La Lucette Sb-Au-(W) vein-deposit (Armorican Massif, France): new time and genetic constraints to decipher the 310-295 Ma Sb-Au metallogenic peak in the Variscan Belt

Florent Cheval-Garabédian[1-2*], Eric Marcoux[1], Hugues Raimbourg[1], Michel Faure[1]

1: Institut des Sciences de la Terre d'Orléans (ISTO), UMR 7327-CNRS/Université d'Orléans/BRGM, 1A Rue de la Férollerie 45071 Orléans Cedex 2, France

2: Present address: EQIOM, 10 avenue de l'Arche, 92419 Courbevoie, France

* Corresponding author: florent-cg@hotmail.fr

Abstract

In the French Armorican Massif, La Lucette is the most important late Variscan Sb deposit with an uncommon Sb-Au-(W) ore. Detailed mineralogical investigations, fluid inclusion study in gangue and ore combined with *in-situ* apatite LA-ICP-MS U/Pb dating were carried out to decipher the Sb-Au-W relationships, and metallogenic processes. The mineralization consists of sigmoidal quartz lenses. Four stages of ore deposition have been identified, consisting in the following mineral assemblages: i) scheelite, ii) arsenopyrite, pyrite, iii) base-metals and iv) stibnite-Au. An initial aqueous-carbonic hot-fluid (350 to 250 °C) from a metamorphic source is involved for the early scheelite to base-metals stages, and fluid/rock interaction could be responsible for the scheelite crystallization. Cooling and mixing of the initial fluid with an aqueous cold meteoric fluid (~200 to 130 °C), are key factors for the late Sb-Au ore-deposition. P-T conditions express a shallow emplacement level (3.5 to 6 km) in a single and progressive crystallization-deformation event. No significant exhumation, and no additional magmatic source from late Variscan felsic or early Carboniferous mafic magmatic events are needed for the Sb-Au-(W) ore genesis. Structural features and new LA-ICP-MS U/Pb apatite dating associated with a regional synthesis show that all major Sb-Au mineralizations of the Armorican Massif, and most from the European Variscan Belt districts have a relatively similar genetic model. In the French Variscan massifs those deposits have been emplaced during the same mineralizing peak, which operated at around 310-295 Ma, and was controlled by the late-orogenic Variscan post-thickening tectonic event.

Keywords. Sb-Au deposit, Tungsten, Armorican Massif, La Lucette deposit, Orogenic-gold, Variscan belt

1. Introduction

Antimony (Sb) is classified by the European Union as a highly critical metal for the economy and for the energetic transition. Shear zones-hosted Sb quartz vein-type deposits are the most important source of Sb worldwide (Schwarz-Schampera, 2014). The main Sb-metallogenic province is South China (Peng et al., 2005; Yan et al., 2022; Zhang et al., 2022; Zheng et al., 2022). Moreover, Sb and gold (Au) bearing quartz vein-type (Sb-Au), and monotonous Sb-As quartz vein-type were recognized and mined since the antiquity in the European Variscan belt (Wagner and Cook, 2000; Bellot et al., 2003; Akçay et al., 2006; Dill et al., 2008; Neiva et al., 2008; Schwarz-Schampera, 2014; Epp et al., 2019). They are widespread in the Bohemian Massif (Němec and Zachariáš, 2018), Rhenish Massif, the Schwarzwald in Germany (Dill, 1985; Wagner and Cook, 2000; Epp et al., 2019), the French Massif Central (FMC; Périchaud, 1980; Munoz and Shepherd, 1987; Bril and Beaufort, 1989; Bellot et al., 2003; Bouchot et al., 2005), and the Armorican Massif (Serment, 1978; Fouquet, 1980; Marcoux et al., 1984 ; Chauris and Marcoux, 1994; Bailly et al., 2000; Pochon et al., 2018; Cheval-Garabédian et al., 2020a). Some Sb-Au deposits show a peculiar association with a tungsten ore (Sb-Au-(W) deposits), such as in the Iberian Massif (Gumiel and Arribas, 1987; Neiva et al., 2008), Slovakian Western Carpathians (Chovan et al., 1995, 1998), and in the La Lucette district (Serment, 1978) in the Armorican Massif (AM). However, those studies are typically focused on the Sb and Au ore-genesis, ignoring the potential economic W ore content and its relationship with Sb and Au resources.

The Armorican Massif (AM) represents the first metallogenic province for Sb-Au and Sb-As deposits in France according to its historical production (around 130 000t Sb metal between 1860 and 1991) and its largest Sb potential resources, mainly known in the Vendée and Quimper

districts (Fig. 1; Audion, 2012; Cheval-Garabédian, 2019). Despite the highly economic interest and long-time mining history, the formation of the Sb-Au deposits is still disputed. In particular, 1) the age of the Sb-Au hydrothermal event(s), 2) the temporal and genetic links between the regional episodes of magmatism, deformation and other hydrothermal mineralizations are still pending questions.

Previous works on the Quimper (Fouchet, 1980), Vendée (Marcoux et al., 1984), and La Lucette Sb-Au-(W) (Serment, 1978; Guiollard, 1995) districts suggest an emplacement age around 300 Ma coeval with the end of syn-tectonic leucogranitic magmatism, and a genetic link between these mineralizations and magmatic fluids (Chauris and Marcoux, 1994; Bouchot et al., 1997). However, the timing of Sb-Au deposits is only constrained by relative datings, and no magmatic-ore-fluid signatures have been recognized, yet in the Central part of the AM (Fig. 1). Recent works with indirect absolute dating on base metal-Sb ± Au occurrences from the Saint-Aubin-des-Châteaux (e.g. illite from the ore assemblage, Pochon et al., 2019), and the Semnon Sb-Au deposit suggested a Sb-Au main hydrothermal peak at ca. 360 Ma (Pochon et al., 2018). Ore-fluids were suggested as coeval with the mafic-doleritic magmatism during the early variscan compressive tectonics (Pochon et al., 2016, 2018, 2019). This genetic relationship is not yet demonstrated by a clear continuity from magmatic to hydrothermal processes. Moreover, fluid inclusions studies did not highlight a magmatic origin. In the southern part of the AM, or Ligerian domain, recent works on Sb-As quartz-veins from the La Bellière district (Fig. 1) suggest a late-Variscan emplacement, assisted by metamorphic-meteoric ore-fluid circulations coeval with strike-slip movements along the South Armorican Shear-Zones (Cheval-Garabédian et al., 2020a).

The La Lucette Sb-Au-(W) district with its eponym deposit, located in the North-Armorican Domain is a good target to address these questions (Fig. 1, 2). This deposit was the first French Sb deposit and the second Au one in the AM in terms of production. It is closely spatially

associated with doleritic dykes emplaced at 360 Ma (Pochon et al., 2016; Fig. 2), and with major shear-zones. At a more regional scale the study area is close to the felsic-magmatism of Le Pertre leucogranite (Fig. 1, 2) which is dated at ca. 340 ± 2 Ma (U/Pb on zircon, Cocherie, 2007; Vernhet et al., 2009). The paragenetic evolution of the Au and its relationship with Sb ore are not clearly documented, and the atypical economic scheelite high grade-co-product discovered in the Sb-Au ore during the exploration campaigns in the 70's (Serment, 1978) remains unstudied.

In this study, detailed textural-mineralogical investigations with fluid inclusions study in gangue and ore minerals, and *in-situ* apatite LA-ICP-MS U/Pb dating, were carried out in the La Lucette Sb-Au-(W) deposit to decipher the mineralogical and hydrothermal evolution responsible for the ore formation, and its time relationships with Carboniferous tectonics, magmatism, and hydrothermal events of the Variscan AM. This will led us to propose a new metallogenic model for the Sb-Au quartz vein deposits in the AM.

2. Geological and metallogenic background

2.1 The Laval Basin in the Armorican Massif framework

The major La Lucette district is hosted in the early Carboniferous Laval Basin which belongs to the southern part of the North Armorican Domain (NAD) (Fig. 1, 2). Together with the Central Armorican domain, the NAD consists of gently folded and unmetamorphosed early Paleozoic formations (from Cambrian to Carboniferous) unconformably overlying Neoproterozoic series of greywacke and shale deformed during the Ediacaran Cadomian orogeny. The Central and North Armorican domains correspond to a Gondwana-derived microcontinent (i.e. Armorica) that collided with the Northern Gondwana margin and the

Saxothuringian domain to the south and north, respectively (e.g. Matte, 1986; Faure et al., 2005, 2008; Ballèvre et al., 2009). This collision recorded during the late Devonian-early Carboniferous at 360-350 Ma was followed by the development of crustal-scale dextral shear-zones, namely the North-Armorican-Shear-Zone (NASZ), and the South-Armorican-Shear-Zone (SASZ; Fig. 1). The Variscan cycle ended by a late- to post-orogenic extensional episode around 320-290 Ma, coeval with dextral shearing and syntectonic felsic magmatism (Tartèse et al., 2011; Ballouard et al., 2017, and references within; Dusséaux et al., 2019; Dusséaux et al., 2022).

The NASZ bounds the southern edge of the Laval basin and separates the NAD from the CAD (Fig. 1, 2, 3). Ductile to brittle dextral strike-slip movements developed during the late Carboniferous time (Watts and Williams, 1979; Gumiaux et al., 2004). The Laval basin is interpreted as a pull-apart basin opened during a transtensional stage, then the sedimentary series were folded and thrusted to the north during a transpressional phase (Houlgatte et al., 1988). The substratum basement of the Laval basin consists of Neoproterozoic and earlyCambrian metasedimentary formations (Fig. 2, 3) weakly metamorphosed in the green-schist facies during the Cadomian orogeny intruded by the Alexain and Fougères granites and granodiorites at 540 ± 10 Ma (U/Pb on monazite; Pasteels and Doré, 1982; Graviou et al., 1988), and unconformably covered by early Cambrian series (Bonjour et al., 1988; Guerrot et al., 1992).

The filling of the Laval basin started by the deposition of an early Ordovician quartzite (regionally known as the “Armorican quartzite” formation; Houlgatte et al., 1988; Le Gall et al., 2011). Then, a continuous sequence of marine sediments was deposited up to the middle Devonian. A middle to late Devonian hiatus, is ascribed to erosion during the late Devonian

"Bretonnian phase". The early Carboniferous sedimentary formations, displaying strong lateral facies variations, unconformably overlaid the previous series (Houlgatte et al., 1988; Le Gall et al., 2011). During the Serpukhovian-Bashkirian, the Laval basin was deformed by north-verging folds with N120°E axis associated with a N100-120°E axial planar cleavage (Le Gall et al., 2011). Thin coal-bearing layers, coeval with continental terrigenous sedimentation, unconformably deposited during the Gzhelian (310 to 300 Ma). A network of post-Gzhelian conjugate NW-SE and NE-SW fractures crosscut the entire AM (Fig. 1,2).

The Paleozoic magmatism is rare in the Laval basin (Fig. 1, 2). A widespread swarm of dolerite dykes and sills have crystallized at ca. 360.0 ± 4.2 Ma (U/Pb on apatite; Pochon et al., 2016; Fig. 2). Three acidic volcano-sedimentary episodes represented by rhyolite and ignimbrite occurred during the Tournaisian (Fig. 2; Le Gall et al., 2011). The younger felsic magmatic episode is represented by the Pertre leucogranite and associated dykes swarm, dated at 340 ± 2 Ma (U/Pb on zircon; Vernhet et al., 2009 and enclosed references). This syntectonic magmatic event is controlled by the dextral-strike-slip activity along the NASZ (Vernhet et al., 2009). Furthermore, a late Carboniferous felsic magmatic event, widespread in the AM at ca. 320-300 Ma, is notably expressed by the emplacement of the Lizio leucogranite (Tartese et al., 2011) and Pontivy-Rostrenen magmatic complex (Ballouard et al., 2017) (Fig. 2). However, such magmatism is not documented in the study area.

2.2 The La Lucette Sb-Au-(W) deposit

2.2.1 Mining history and Sb-Au production

In the La Lucette district, only its eponym deposit has been intensively mined. The other occurrences such as those around the Port-Brillet town (Fig. 3A) have been artisanaly mined with no significant production. In the NE of the Port-Brillet town, some Hg-Sb stratiform mineralizations are spatially associated with iron and coal occurrences (Fig. 3A; Le Gall et al., 2011). The La Lucette deposit has been fortuitously discovered in march 1891, and the ore has started to be extracted in April 1899 (Guiollard, 1995). The underground mining works allowed the discovery of the Henri and Mazure veins (Fig. 3B). The greatest exploitation period began in 1900 with the discovery of the Georges vein, the richest of the deposit. Between 1908 and 1909, the La Lucette deposit alone has secured 25 % of the Sb world demand and was the largest Sb deposit in the world (Guiollard, 1995). Au ore has been found in 1903 and started to be mined in 1909. During the first World War the discovery of the Wilson and Z veins (Fig. 3B) was at the origin of a second but slower exploitation period, before the closure of the mine in 1934. Overall, 42 000 t of Sb metal with 8.7 t of Au have been produced (Serment, 1978; Guiollard, 1995; Bouchot et al., 1997). It is still ranking among the 30-world major Sb vein-type deposits. The La Lucette deposit is by far the French largest Sb deposit, and also the second historical Au producer of the AM, behind the la Bellière deposit (Cheval-Garabédian et al., 2020a). The associated tungsten ore has been discovered in the new Sb-Au quartz-veins from the oriental part of the La Lucette mine, during the exploration campaign led by the French Geological Survey (BRGM) between 1974 and 1979 (Serment, 1978). Their economic potentials remain poorly constrained.

2.2.2 The Sb-Au mineralization

The study area is located between the Gzhelian S^{t}-Pierre-la-Cour coal basin and the Tournaisian-Visean Laval basin (Fig. 2, 3A). All Sb-Au-(W) vein-type deposits and

occurrences are located close to the regional N100-120°E Misedon antiform (Fig. 3). The core of the anticline is occupied by the early Ordovician quartzite surrounded by the early Silurian sandstone formation and by the late Silurian alternations of black-shale and sandstone (Fig. 3). The folding is older than the mineralized event and acted only as a regional structural trap (Fig. 3; Douxami, 1907; Serment, 1978). The major La Lucette Sb-Au-(W) deposit consists of a dozen of quartz vein structures striking NE-SW (N0°E to N40°E), steeply dipping between 65 to 85° to the SE (Fig. 3C), perpendicularly to the anticline axis. The mineralized quartz veins display a pinch-and-swell morphology with a variable thickness between 0.3 to 4.0 m, with an average of 0.8 m (Douxami, 1907). The Sb-Au ore has been mined until the depth of -260 m, and the structures remain opened at depth (Serment, 1978).

The Sb-Au-(W) quartz veins are mainly hosted in the late Silurian micaceous quartzite and black shale formation (Fig. 3A, C). All veins crosscut the regional cleavage (Douxami, 1907). The Sb-Au-(W) ore is trapped in the quartz and carbonate veins along a brittle fault zone infilled by brecciated and altered rocks showing hydrothermal bleaching, and silicification (Douxami, 1907; Serment, 1978).

Sb grades vary between 10 to 50 % Sb (Guiollard, 1995). In the ore, Au grades are also very rich with an average value between 30 to 40 g/t Au, although characterized by an irregular distribution. In the ore, high grade-Au is preferentially i) associated with arsenopyrite, ii) in free grain in the quartz gangue, or iii) associated with stibnite (Machairas, 1974; Serment, 1978). On the contrary at the mine-scale, high-grade Au seems to be correlated with low-Sb-grade (Serment, 1978). Scheelite has been identified in the BRGM drill cuttings with economic grades ranging from 0.22 to 1.08 % WO_3 over 2.4 m (Serment, 1978).

The ore mineralogy is mainly represented by stibnite, arsenopyrite, pyrite, visible native gold, and minor chalcopyrite, sphalerite, marcasite, zinkenite, gersdorfitte, chalcostibnite, galena,

tetraedrite, aurostibite, scheelite and jamesonite (Machairas, 1974; Serment, 1978: Chauris and Marcoux, 1994; Bouchot et al., 1997; Pochon, 2017). Even if all the authors agree for a late stibnite precipitation, the paragenetic succession is still unclear as well as the precise position of Au and scheelite in the crystallization sequence. The stibnite is present either as pluri-decimetric lamellar mass infilling geodic quartz or as dissemination in the quartz gangue (Machairas, 1974; Serment, 1978). The fluid inclusions study of Pochon (2017) suggests a wide-range of trapping temperatures around 300 ± 80 °C, and a precipitation mechanism associated with a potential aqueous-carbonic fluid cooling and/or

Fluid unmixing.

3. Materials

3.1 Petrography and EMPA analyses

Samples from La Lucette deposit were taken from different parts on the main mineralized veins and come from the rock collection of the Paris 6 University, and from the Museum of the Ecole des Mines de Paris (Mines ParisTech). The accessory mineral phases were identified using a Merlin compact Zeiss Scanning Electron Microscopy (SEM), co-operated by BRGM-CNRS-Orléans University, and equipped with Energy Dispersive System (EDS) for qualitative analyses. In addition, SEM-cathodoluminescence imaging has been made using a MEB-CL MIRA-3 Tescan (BRGM-CNRS-Orléans University). Chemical analyses of ore minerals were obtained with the Cameca SX-Five Electron Probe Micro-Analyzer (EPMA) at the Institut des Sciences de la Terre d'Orléans (ISTO). The sulfides analyses were performed using an accelerating voltage of 20 kV, a beam current at 40 nA, a beam diameter of 3 µm, and a counting time of 30 s for Fe, Ni, Co, Sb, Pb, Cu, As, Zn, Ag, Bi, and 60 s for Au (detection limit around 800 ppm). The carbonates were analyzed using an accelerating voltage of 15 kV, a beam current of 6 nA, a beam diameter of 3 µm, and a counting time of 10 s for Si, Fe, Mn, Mg, Ca, Sr

following themethodology of Poitrenaud (2018). Details on the method, parameters and analytical data are given in ESM1.

3.2 U/Pb dating

U/Pb dating on hydrothermal apatite from the mineralization was conducted *in-situ* by laser ablation inductively coupled plasma mass spectrometry (LA-ICP-MS) at the GeOHeLiS analytical platform (Géosciences Rennes/OSUR, Univ. Rennes) using an ESI NWR193UC Excimer laser coupled to an Agilent 7700x quadrupole ICP-MS equipped with a dual pumping system to enhance sensitivity (Paquette et al., 2014). The analytical procedure followed the method described in Pochon et al. (2016). Details, standard analyses and analytical data are provided in ESM2. All errors are listed at 2σ level and in percentage. Concordia diagrams and calculated ages have been produced using IsoplotR (Vermeesch, 2018).

3.3 Fluid inclusions study in gangue and opaque ore minerals

Fluid inclusions study has been performed on 150 µm-thick doubly polished thin sections. Fluid inclusions typology and petrography have been carefully investigated in order to assess the relationship between, fluid inclusions, quartz generations, and respective locations in the ore-paragenetic succession.

Microthermometric study on fluid inclusions trapped in the quartz gangues and scheelite was carried out using a heating-freezing Linkam THMS 600 system equipped with a Leica DM 2500 M transmitted optical microscope at the ISTO laboratory in Orléans. The microthermometric study of the fluid inclusions trapped in stibnite was performed under infrared light microscopy (IR) using a U.S. Geological Survey heating-freezing system mounted on an Olympus BHSM infrared microscope at the BRGM in Orléans. The obtained

image is transmitted to a black and white monitor via a high-resolution infrared camera (Hamamatsu) that allows observations in the near infrared to wavelengths of $\lambda \leq 2.5$ nm (Bailly et al., 2000). The microthermometric measures have been done under a constant intensity light source, close to the minimal to avoid an overestimation of the salinity (Moritz, 2006). Fluid inclusions on La Lucette are difficult to measure due to their small size (around 8 µm), and the poor transparency of the gangue and stibnite.

The two heating-freezing systems were calibrated using 4 standards Syn Flinc fluid inclusions, including a CO_2-H_2O fluid inclusions with a CO_2 melting temperature at − 56.6 °C, a pure H_2O fluid inclusions with ice melting temperature at 0 °C, a melting temperature of clathrates from CO_2-H_2O fluid inclusions at 10 °C, and a critical homogenization temperature of pure H_2O fluid inclusions at 374.1 °C. This calibration has been carried out several times to ensure the good reproducibility of the results. The microthermometric results have a precision of ± 0.1 °C for the temperature below 50° with the Linkam system, and ± 0.4 °C with the IR USGS system. For the temperature above 100 °C the uncertainty of the temperature of the 2 systems is ± 1 °C. The results obtained by the 2 methods are consistent and reproducible. The cycling method (Goldstein and Reynolds, 1994) was used for the measures of the ice melting temperature for the fluid inclusions in the stibnite to obtain a better precision.

Degree of fill (F) is estimated as liquid / vapor + liquid ratio at ambient temperature. The volatile phase of the H_2O-CO_2-NaCl inclusions is dominated by CO_2 which can reach 99.7 mol% with some traces of CH_4 and N_2, according to the Raman spectrometry analysis on three-phase fluid inclusions performed by Pochon (2017). The data of Bakker (1999) were used to estimate the composition and molar volume of the volatile phase of the aqueous-carbonic inclusions in the pure H_2O-CO_2-NaCl system, neglecting the traces of CH_4 and N_2. Because of the highly H_2O

composition of the inclusions, the salinities were calculated as wt percent NaCl equivalent using the equations of Bodnar (1993) for aqueous fluids and for aqueous-carbonic fluids. Due to the incorporation of H_2O in the gas hydrate (for aqueous-carbonic fluids), the salinities calculated are higher than the real salinities (Collins 1979). The isochores were calculated using the program ISOC from the computer package FLUIDS-1 (Bakker, 2003) using the equations of Zhang and Frantz (1987) and Bakker (1999) for the H_2O-NaCl, and H_2O-CO_2-NaCl systems, respectively.

4. Mineralogy of the Sb-Au-(W) La Lucette deposit

4.1 The mineralized facies

At macroscopic scale, the ore-vein-samples from La Lucette deposit show a same pattern from the wall-rocks to the core of the vein system. The wall-rocks of the veins are occupied by a brecciated facies composed of highly fractured micaceous sandstone of dark beige color, or of indurated black-shale (Fig. 4A, C, D). The clasts of country-rocks display angular shapes with a reduced displacement, and local puzzle-like textures (Fig. 4A; Jébrak, 1992; Jébrak, 1997). The country-rock clasts are cemented by an early milky and comb quartz generation (Qz1 in Fig. 4) with coarse greyish carbonates in it (Fig. 4 C, D). Towards its core, the vein is formed by massive quartz displaying a limpid and comb habitus (Qz2; Fig. 4A). The stibnite precipitation seems to be contemporaneous with the Qz2 and shows centimetric-scale rods shapes. Au grains are spatially associated with stibnite in the cataclased early milky quartz (Fig. 4B, Qz1). Coarse cm-scale scheelite has been observed in the brecciated facies within the Qz1. In the core of the vein, the initial scheelite is highly fractured and cemented by stibnite (Fig. 4C, D).

On the basis of gangue and ore mineral textural observations, four stages have been recognized and are described below, namely: i) stage 1 with early tungsten, ii) stage 2 with arsenic and iron, iii) stage 3 with base metals, and iv) stage 4 with Sb and Au. The Figure 8 summarizes this paragenetic sequence.

4.2 Stage 1: early tungsten

The beginning of this stage corresponds to the deposition of coarse euhedral scheelite (up to 1 cm in size) in a macrocrystalline Qz1 quartz (crystal size > 500 µm; Fig. 5A, B). Quartz 1 displays a blocky habitus with regular growth bands, without significant deformations (Fig. 5B), and numerous fluid inclusions. The euhedral shape and straight grain boundaries between scheelite and Qz1 suggest both minerals are coeval. This quartz generation corresponds to the milky quartz (Qz1;(Fig. 4).

Apatite crystals have been observed for the first time in the quartz vein gangue by SEM-BSE imagery (Fig. 5C). They display a sub-euhedral shape with variable grain-size, with an average of 30 µm, and up to 100 µm. Apatite crosscuts and cements the scheelite. Some scheelite clasts are observed in apatite (Fig. 5C), asserting that apatite deposition occurred after scheelite. Its more accurate position in the paragenetic succession remains difficult to estimate. No complex zoning has been identified both in apatite and scheelite.

4.3 Stage 2: arsenic and iron

The beginning of stage 2 is marked by a discrete episode of brittle fracturing and deposition of the second quartz generation (Qz2). Quartz 2 crystals exhibit a microcrystalline grain-size (< 100 µm in size) without evidence of any ductile deformation (no bulging, subgrain rotation recrystallization; Fig. 5D, E). Their rounded edges and interpenetrated grains, correspond to a

mosaic quartz texture (Fig. 5D, E; Bouchot et al., 1994; Dong et al., 1995). This brittle fracturing episode is coeval with the crystallization of arsenopyrite and pyrite. Arsenopyrite forms small rhombic crystals with needle shape (< 100 µm in size), aggregates (up to 100 µm) or can be associated with subhedral crystals of pyrite (Fig. 5F). Pyrrhotite inclusions are common within arsenopyrite. Pyrite and arsenopyrite are commonly included or are fractured by stibnite aggregates (Fig. 5F).

Arsenopyrite has variable concentrations of Sb and As (see ESM 1 for detail). Arsenic concentration ranges from 41.5 to 43.6 wt% (29.2–31.2 at% As) with an average value of 42.4 wt% (30.0 at% As). Sb content ranges from 575 ppm to 0.8 wt% but Co and Ni contents are under the detection limit of the method (< 700 ppm). Au has been detected only in one analysis, more likely corresponding to a Au inclusion rather than refractory Au. Assuming the arsenopyrite-pyrite-pyrrhotite equilibrium, the calculated formation temperature is around 345 °C (mean of analyses) with a range between 330 and 370 °C.

4.4 Stage 3: base metals

This stage is very discrete in the ore. It is marked by a new undeformed quartz generation (Qz3) surrounding or crosscutting Qz2 (Fig. 5E, F and 6A, B). The macrocrystalline (> 200 µm) Qz3 displays a euhedral shape with a dark-color core noted Qz3A caused by a high proportion of fluid inclusions. It presents a more hyaline aspect towards its edges near the contact with the stibnite (noted as Qz3B, Fig. 5E, F and 6A, B). Sphalerite is the dominant mineral species of this stage. It occurs as anhedral rounded shape crystals up to 200 µm in size, either isolated or with a dendritic shape in the Qz3 quartz (Fig. 6A, B), indicating a slightly later crystallization than Qz3. Sphalerite and chalcostibite commonly show clasts of arsenopyrite with dissolved shape (Fig. 6B, C, D), and chalcostibite and zinkenite are frequently associated with it. Chalcopyrite is minor, only observed as small inclusions in sphalerite (Fig. 6D). Tetrahedrite,

famatinite (Pochon, 2017), marcasite and galena (Machairas, 1974) complete this assemblage. Sphalerite chemical compositions are close to the stoichiometric formulae, with a minor enrichment in Fe (average 2.1 wt%; see ESM1 for details) and minor Cd contents (average 0.07 wt%).

4.5 Stage 4: antimony and economic gold

This stage begins with a very discrete new generation of quartz (Qz4) that crystallized in epitaxy around the Qz3 (Fig. 7A). The evidence for a coeval deposition between Qz3, Qz4 and stibnite remain difficult to establish. The Qz4 has, a hyaline aspect with few fluid inclusions, and shows well developed growth bands. Massive stibnite is the dominant ore species. It fills the voids formed during the previous stages and corrodes the Qz3 grain boundaries. This mineral species overprints and fills the fractures of all the previous minerals, such as the early scheelite (Fig. 7B), arsenopyrite, and pyrite (Fig. 5F). Stibnite chemical compositions are close to the stoichiometric formulae with homogenous As concentrations from 0.18 to 0.22 wt% averaging at 0.2 wt% (see ESM1 for details).

Abundant iron-dolomite is enclosed in, and contemporaneous with stibnite (Fig. 7C) or occurs in the hydrothermalized wall-rocks. This carbonate species displays euhedral shape up to 1cm in size, and numerous stibnite inclusions (around 10 µm in size) are in its cleavage planes (Fig. 7C). Iron-dolomite has an average composition of 14.2 wt% MgO, 28.8 wt% CaO, 10.9 wt% FeO and 0.1 wt% MnO (n = 55; ESM 1). Zinkenite inclusions appear along stibnite cleavages. Rare ovoidal native Sb micro inclusions (2–5 µm) in the stibnite belong to this assemblage.

Visible Au has been commonly observed in thin-section. Gold patches range between 2 µm to more than 500 µm in size. Gold has not been observed in close spatial association with the

scheelite. Small sized Au inclusions (≤ 10 µm) are within or infill the tiny microcracks fracturing the arsenopyrite and pyrite or are more rarely included in the sphalerite (Fig. 6D). The majority of large-size Au (> 100 µm) intergrowths with the stibnite and displays, i) an anhedral rounded shape (Fig. 7D, F), or ii) a dendritic shape and skeletal edges, supporting a deposition time after the stibnite (Fig. 7E). Rare aurostibite has been observed in association with stibnite and Au (Fig. 7F).

5. LA-ICP-MS U/Pb geochronology on apatite

Our textural study presented in the previous section shows that hydrothermal apatite deposition occurred after the early tungsten stage 1 (Fig. 5C, Fig. 9A, B) of the La Lucette ore. After a careful characterization, 16 apatite grains have been selected for dating (see ESM 2 for analytical details). SEM-BSE images do not show evidence for a complex zoning (Fig. 9 A, B). Between one and eight U/Pb spots have been performed on each grain (Fig. 9A, B). Apatite grains from the La Lucette deposit contain variable amount of common Pb with $^{207}Pb/^{206}Pb$ ratios ranging between 0.1115 and 0.7710. The ellipses plot along a discordia line in a Terra Waserburg diagram that yields a lower intercept date of 299 ± 11 Ma (MSWD = 5; Fig. 9C). The upper intercept yields an initial $^{207}Pb/^{206}Pb$ ratio for the dated apatites at 0.8234.

6. Fluid inclusions study

No solid phases have been observed in the five fluid inclusion (FI) families. In the following, the liquid phase will be noted (L) and the volatile phase (V). Possible primary FI were observed in clusters, isolated grains, or in inclusions plans following the growth bands of the Qz1 (Fig. 10A). Secondary FI are distinguished without ambiguity and are related to fluid inclusion planes crosscutting the grain boundaries (Fig. 10B). The Table 1 summarizes all the microthermometric results FI of La Lucette deposit. The Table 2 summarizes the estimated bulk

densities and bulk compositions of the three-phase aqueous-carbonic FI, calculated only with the microthermometric data. Our microthermometric results obtained in the FI from the quartz gangue match with the data reported by Pochon (2017).

6.1 Aqueous-carbonic inclusions in the Qz1 and scheelite (stage 1)

Two types of aqueous-carbonic FI were identified: i) an abundant two-phase L_{H2O}-L_{CO2} FI population in the Qz1 and scheelite (Fig. 10C), and ii) a more rare three-phase L_{H2O}-L_{CO2}-V_{CO2} FI population at room temperature, only in the Qz1. In the scheelite, primary FI are difficult to identify because of the high proportion of secondary aqueous FI (Fig. 10B).

The L_{H2O}-L_{CO2} FI have a variable volatile phase proportion ranging from 10 to 50% of the total volume of FI. The melting temperature of solid CO_2 (Tm CO_2) could not be observed because of the small size of the FI. The ice melting temperatures (Tm ice) of FI in the Qz1 and scheelite are very similar and ranging from -3.5 to -3 °C and -3.7 to -2.1 °C with an average at -2.9 and -2.8 °C respectively (n=6; Fig. 11A). The presence of a carbonic phase was indicated by the melting temperatures of CO_2-clathrate (Tm Clat), with an average at 9.8 °C (n=6) for those in the scheelite and 9.9 °C for those in the Qz1 (n=6; Fig. 11B). Homogenization temperatures of the carbonic vapor phase (ThCO_2) and additional and separated CO_2 phase were not observed. Final homogenization temperatures (Th) were always to the liquid phase and vary from 246 to 346 °C with an average at 305 °C for those in the Qz1 (n=5), and between 296 to 330 °C with an average at 312 °C for those in the scheelite (n=6; Fig. 11C).

The L_{H2O}-L_{CO2}-V_{CO2} FI were observed only in isolated inclusions and are spatially associated with the L_{H2O}-L_{CO2} FI in the same clusters. The Tm CO_2 could not be observed. The Tm ice has an average at -2.7 °C (n=2; Fig. 11A). Tm Clat were commonly observed at 10.3 °C (n=2; Fig.

11B), with a $ThCO_2$ at 21.9 °C to the liquid phase. The Tm Clat close to 10 °C indicate that the composition of the volatile phase is dominated by CO_2 with a little amount of other gas species such as CH_4 and N_2 (Collins, 1979). The degree of filling of the selected FI ranges between 0.55 and 0.75 with a high bulk density between 0.91 and 0.96 g/cm^3 corresponding to a high H_2O content and a moderated bulk CO_2 content between 0.15 to 0.25 mol %. The salinities of the two- and three-phase FI are moderate and ≤ 5 wt % NaCl equiv.

6.2 Aqueous-carbonic inclusions in the Qz3 (base metals stage 3)

Unambiguous identification of primary inclusions in the Qz3 is difficult. The FI in the Qz3 display the same features as those in the Qz1 and scheelite, with L_{H2O}-L_{CO2} FI spatially associated with L_{H2O}-L_{CO2}-V_{CO2} FI, at room temperature (Fig. 10D, E, F).

In the Qz3A-hosted FI, the Tm CO_2 could not be observed for the L_{H2O}-L_{CO2} FI. The Tm ice ranges from -5.4 to -1.3 °C with an average at -3.5 °C (n=50; Fig. 11A). Tm Clat ranges from 8.8 to 11.0 °C with an average at 10.2 °C (n=48; Fig. 11B). Final Th occurred to the liquid phase between 221 to 311 °C with a main mode at 253 °C (Fig. 11C). The Tm CO_2 and the Th CO_2 could not be observed in the L_{H2O}-L_{CO2}-V_{CO2} FI. The Tm ice ranges from -4.7 to -2.7 °C with an average at -3.5 °C (n=3; Fig. 11A). Tm Clat ranges from 9.6 to 11.2 °C with an average at 10.1 °C (n=48; Fig. 11B) indicating that the composition of the volatile phase is also dominated by CO_2. Final Th occurred to the liquid phase at 271 °C (n=3; Fig. 11C). For all IF trapped in the Qz3A, the salinities remain low and ≤ 5.5 wt % NaCl equiv.

For the FI hosted in the Qz3B (Fig. 9D), the microthermometric results are similar to those in the Qz3A, with L_{H2O}-L_{CO2} FI spatially associated with L_{H2O}-L_{CO2}-V_{CO2} FI at room temperature (Fig. 10D, G, H). Both FI are mainly arranged in inclusion planes interpreted to be pseudo-

secondary. The Tm CO_2 could not be observed for the L_{H2O}-L_{CO2} FI. The Tm ice ranges from -5.4 to -1.4 °C with an average at -3.4 °C (n=39 Fig. 11A). Tm Clat ranges from 8.2 to 11.4 °C with an average at 9.8 °C (n=41; Fig. 11B). Final Th occurred to the liquid phase, between 208 to 339 °C with a main mode at 249 °C (n=24; Fig. 11C).

The Tm CO_2 could not be observed for the L_{H2O}-L_{CO2}-V_{CO2} FI. The Tm ice varies from -4.6 to -2.0 °C with an average at -3.1 °C (n=13; Fig. 11A). Tm Clat ranges from 8.1 to 10.4 °C with an average of 9.5 °C (n=11; Fig. 11B) and remain close to 10 °C, indicating that the composition of the volatile phase remains dominated by CO_2 with a little amount of other gas species such as CH_4 and N_2. Rare $ThCO_2$ have been measured at 24.7 °C (n=9), with a homogenization to the liquid phase. Final Th are to the liquid phase between 237 to 305 °C with a main mode at 262 °C (n=9; Fig. 11C). The degree of filling of the of the selected FI is lower than FI of the stage 1, and ranges between 0.62 to 0.68 with a bulk density slightly lower between 0.91 to 0.94 g/cm^3 corresponding to a dominant H_2O content and a low bulk CO_2 content between 0.18 to 0.19 mol %. The salinities of the two- and three-phased FI trapped in the Qz3B remain in the range of the FI measured in the previous quartz generations, ≤ 5 wt % NaCl equiv. One-phase L_{CO2} FI are associated with the L_{H2O}-L_{CO2}-V_{CO2} and L_{H2O}-L_{CO2} FI but they were too tiny to be correctly observed and measured.

6.3 Aqueous inclusions in the stibnite (Antimony and gold stage 4)

Two-phase aqueous inclusions L_{H2O}-V_{H2O} are documented in stibnite as homogeneous populations. The vapor phase occupies approximately 20 to 30 % of the total volume of FI. They display a tubular shape, with an average of 25 µm in size, and are oriented parallel to the {110} and/or {010} stibnite crystallographic planes (Fig. 10I, J). These primary inclusions occur isolated or in groups of 2 or 3 and are not very abundant. The Tm ice range from -3.3 to -0.3 °C with an average at -2.2 °C (n=11; Fig. 11A). Final Th occurred to the liquid phase

between 190 to 200 °C with an average at 195 °C (n=2; Fig. 11C). The salinities are relatively low ranging from 0.5 to 5.4 wt % NaCl equiv with an average at 3.6 wt % NaCl equiv.

6.4 Aqueous secondary inclusions in the scheelite

Secondary two-phase aqueous FI, L_{H2O}-V_{H2O} are conspicuously observed in scheelite (Fig. 10B). They show a small size (< 10 µm), oval-shape and the vapor phase occupies approximately 10 to 50 % of the total volume of the inclusion. They are arranged in inclusion planes following late microcracks crosscutting both the scheelite and the quartz. Secondary monophase-liquid aqueous FI, L_{H2O} are spatially associated with L_{H2O}-V_{H2O} FI (Fig. 10B). The Tm ice of the L_{H2O}-V_{H2O} FI ranges from -2.1 to 0.2 °C with an average at -1.7 °C (n=18; Fig. 11A). The Tm Clat have not been observed. Final Th occurred in the liquid phase between 133 to 185 °C with a main mode at 173 °C (n=17; Fig. 11C). The L_{H2O} FI show similar Tm ice than the L_{H2O}-V_{H2O} FI, ranging from -2.0 to -1.3 °C with an average at -1.5 °C (Fig. 11B). The salinities are relatively low ranging from 0.3 to 3.6 wt % NaCl equiv for the L_{H2O}-V_{H2O}, and between 2.3 and 3.4 wt % NaCl equiv for the L_{H2O} FI.

7. Discussion

7.1 Nature and temperature evolution of the ore-fluid system

The initial vein opening is coeval with the crystallization of high grade scheelite ore within the underformed comb quartz gangue Qz1, (stage 1**;** Fig. 8) and crystallized from a hydrothermal ore fluid enriched in W. FI analyses from both Qz1 and scheelite show a similar behavior. They point to an initial hot aqueous-carbonic fluid type dominated by H_2O and moderated bulk CO_2

content, between 0.15 to 0.25 mol %, with minor admixture of N_2 and CH_4, according to our Tm Clat close to 10 °C (Collins, 1979) confirming the observations from Pochon (2017). According to the same author, the concentrations of the volatile phase in the aqueous-carbonic L_{H2O}-L_{CO2} and L_{H2O}-L_{CO2}-V_{CO2} FI are between ~0 to 27.7 % mol N_2 and between ~0 to 4.6 % mol for CH_4. The high N_2 concentrations have been measured locally. The minimal trapping temperatures range is between 300 °C and 350 °C, while the fluid has a moderate salinity ≤ 5 wt % NaCl equiv (Fig. 11, 12 and Table 1). These features argue for a crustal fluid signature, probably derived from a metamorphic source (Boiron et al., 1990, 2003).

A brittle deformation episode marks the onset of stage 2 (Fig. 8). The crystallization of microcrystalline Qz2 was coeval with the arsenopyrite, pyrite and apatite assemblage. Sb-rich arsenopyrites suggest that Sb was already enriched in the hydrothermal fluid. In the absence of FI analyses for the stage 2, the temperature of formations has been estimated between 330 and 370 °C using the arsenopyrite geothermometer. According to Kretschmar and Scott (1976), and Sharp et al. (1985), the use of the arsenopyrite chemical compositions to assess ore formation temperatures may be considered with caution in our case, because of the presence of minor elements. Compared to the FI data from the stage 1, an overestimation of the temperature of formation of the stage 2 is suspected (Fig. 12A). Nevertheless, the temperature of crystallization remained elevated as those of the Stage 1 (table 1). This mineral assemblage might have precipitated from the same initial hot aqueous-carbonic fluid type without compositional sharp change.

The onset of stage 3 (Fig. 8) corresponds to another brittle fracturing episode, followed by the deposition of a new comb Qz3 with discrete sphalerite with native Au, and chalcostibite. The FI in the core and border of the Qz3 suggest that the hydrothermal system remained globally unchanged. However, we can observe a slight cooling of the system down to 250 °C. The salinity remained moderate, ≤ 5 wt % NaCl equiv.

The final stage 4 (Fig. 8) corresponds to the major economic emplacement of the Sb and Au ore (Fig. 7C). The massive crystallization of stibnite infilling the porosity of the gangue was followed by the deposition of the native Au. The primary FI from the stibnite itself, and the secondary FI in scheelite display close features that prove that a distinct fluid type with a cold and only aqueous composition was involved for the stibnite and Au deposition. At this stage, the minimal trapping temperatures of FI range from 200 to 130 °C, with a main mode at 175 °C (Fig. 11, 12A), and an average salinity slightly lower than that from the previous stages at 3 % NaCl equiv. The low temperatures coupled to the only aqueous character and low salinities of FI argue for a superficial and meteoric origin for this late fluid (Boiron et al., 2003).

The Th versus Tm ice diagram (Fig. 12A) illustrates a general cooling evolution trend showing an initial fluid trapped at relatively high temperature conditions up to 300 °C, which evolved continuously toward a late fluid trapped at lower temperature around 175 °C, and relatively lower salinity during the stage 4. Mineralogical textural and FI investigations are consistent with each other and argue that the apparent polyphase paragenetic evolution can reflect a continuous evolution of a single hydrothermal system, rather than several disconnected contrasting episodes of ore deposition.

Our FI results indicate that the enclosing quartz gangue (Qz3) does not reflect the conditions of the Sb-Au ore deposition, as demonstrated in other Sb-As or Sb-Au vein-deposit studies (e.g. Luders, 1996; Bailly et al., 2000; Wei et al., 2012; Zhu and Peng, 2015; A'xiang and Jiantang, 2018). The previous FI study of La Lucette deposit (Pochon, 2017) only dealing with the quartz gangue has led to propose an incomplete metallogenic model in which the late cold aqueous fluid was considered as disconnected from the Sb-Au mineralization. Our results confirmed the use of the IR microthermometry for FI trapped in opaque minerals such as stibnite, to decipher without ambiguity the hydrothermal history of complex polyphased hydrothermal mineralizations such as the Sb-As or Sb-Au-vein types.

7.2 Pressure and depth estimations

Textural evidences in all stages, and the microcrystalline Qz2 from the stage 2 is contemporaneous with the deposition of the needle-shaped arsenopyrites and indicate a crystallization from a siliceous gel during an episodic pressure drop (Boiron et al., 1989; Wu et al., 1990; Bouchot et al., 1994). It led us to propose that the ore-fluids were likely trapped under a predominantly hydrostatic regime (Scholz, 1988). The temperature corrections due to pressure conditions are very low and the trapping temperatures can be considered as roughly similar to the homogenization temperatures (André-Mayer et al., 2002).

The set of isochores from the aqueous-carbonic FI from stages 1 and 3 are very similar (Fig. 12B) and intersect the geothermal gradients at 50-40 °C/km, twice higher than an average crustal geotherm. The associated trapping temperatures are estimated at about 250-300 °C with pressures from 145 to 186 MPa (lithostatic). This estimated range of pressures indicates a possible paleodepth at around 6 to 5 km during the stages 1 and 3 without significant change in terms of fluid circulation depths.

The isochores from the only aqueous FI from the Sb-Au stage are presented in the Figure 12B. According to the evidence of trapping under only hydrostatic regime and the meteoric source of fluid (see section 7.1), a geothermal gradient of 30-40 °C/km (hydrostatic), close to the common geothermal gradient is proposed. Those, the associated trapping temperatures are estimated at about140-200 °C with pressure variations from 40 to 65 MPa (hydrostatic). This suggests a shallow depth of emplacement between 3.5 to 6 to km for the Sb-Au mineralizations, and that no additional heating source is needed to account for the ore genesis.

The comb, geodic, microcrystalline quartz textures, without deformation, are very similar to the open-space vein infillings (Jébrak, 1992; Bouchot et al., 1994; Bons et al., 2012) observed

in shallow depth vein deposits (e.g. Dowling and Morison, 1988; White and Hedenquist, 1990; Dong et al., 1995; Kontak et al., 1996; Simmons et al., 2005; Chauvet et al., 2006). This supports our FI interpretations and a shallow crustal level of deposition for the La Lucette deposit, below 5-6 km, in brittle deformation conditions.

Those P/T and depth interpretations are consistent with the regional geological background. The eastern NAD neither experienced important crustal thickening nor major exhumation processes during the Variscan orogeny (Gumiaux et al., 2004; Le Gall et al., 2011). The maximal regional metamorphism conditions have not exceeded the green schist facies, with a maximal temperature estimated around 300-400 °C for a lithostatic pressure not exceeding 200 MPa, that corresponds to an estimated depth around 6 km (Le Gall, 1993; Houlgatte et al., 1988; Le Gall et al., 2011). It confirms that the hydrothermal system of the La Lucette ore deposit did not experienced a strong exhumation rate during its evolution. One isochore from the stage 1 records an entrapment pressure higher than the maximal regional metamorphism conditions (Fig. 12B). It could suggest a supralithostatic fluid overpressure condition that is consistent with the textural evidences of pressure drop, in response to the opening of the vein system at the beginning of all ore stages.

Our study cannot provide enough strong results to characterize the pressure and depth conditions from the As-Fe stage 2, but we assume that at least, it should be close to the conditions of the stages 1 and 3.

7.3 Mechanism of the vein formation and stibnite-gold ore deposition

The synchronism between brittle fracturing, controlled by the variations of the shear stress, fluid pressure, porosity increase and ore deposition in open-space vein infilling likely results from a seismic activity (Fig. 13). The shallow emplacement depth documented here leads us to suggest that the ore-vein formation of the La Lucette deposit could be due to a suction pump mechanism (Sibson, 1987). The fracturing episodes reported at the beginning of the different ore-stages could have allowed a connection to the surface synchronous with the main economic-ore deposition stages (Fig. 12B, 13). This process enhanced the progressive cooling and dilution of the initial hot aqueous-carbonic fluid, by the percolation and the mixing with a late cold meteoric fluid, especially during the Sb and Au stage 4. The gentle exhumation/denudation process recorded by the FI could have also enhance this temperature decrease. This mechanism is the simplest way to precipitate stibnite because the solubility of Sb decreases when temperature is lower than 250 °C (Williams-Jones and Norman, 1997; Obolensky et al., 2009). Fluid overpressure conditions recorded by the FI during the stage 1 (Fig.12B) and the textural evidence of the gangue could also have play a role in the ore deposition. Unfortunately, we are not enough data to evaluate clearly this point. The coeval deposition of important amount of iron-dolomite could have also triggered an increase in the pH of the fluid enhancing the decrease of the solubility of the precious metals. The simultaneous deposition of stibnite and native Sb indicates that a decrease in the sulfide fugacity should be considered as another effect of the cooling / dilution process.

7.4 Timing and tectonic control of the Sb-Au mineralization in the Armorican Massif

The orientation of the main Sb-Au-(W)-bearing quartz vein structures (Fig. 14A, B) deduced from the underground mining plans (Bellanger, 1921) shows that the ore-veins display a sigmoidal shape (Bons et al., 2012; Fig. 14B) that can be interpreted as tension gashes

developed during dextral movements along N130°E striking strike-slip fault. Such a feature, reported around the La Lucette mine (Fig. 3 and Fig. 14A, B), is consistent with a N05°E maximal horizontal shortening direction (Z1; Fig. 14A, B). At a regional scale, dextral brittle motion compatible with the NASZ and SASZ between 315 to 295 Ma is documented in the entire AM (e.g. Berthé et al., 1979; Jégouzo, 1980; Jégouzo and Rosello, 1988; Rolin and Colchen, 2001; Gumiaux et al., 2004; Lemarchand et al., 2011; Tartèse et al., 2011; Ballouard et al., 2017).

The hydrothermal apatite grains from the stage 2 of the La Lucette deposit yield LA-ICP-MS U/Pb age of 299 ± 11 Ma which is interpreted as the emplacement age of the Sb-Au-(W) deposit. This late Carboniferous age supports a Sb-Au-(W) mineralizing event around 300 Ma in the NAD accommodated by a dextral strike-slip tectonic regime controlled by a regional N-S maximal horizontal shortening direction.

The main Sb-As and Sb-Au districts in the AM exhibit similar tectonic controls, and relative chronological features are similar to the La Lucette district (Fig. 14A, C). In the Quimper district, the shortening direction is oriented N30-20°W (Fouquet, 1980). The Sb-As veins crosscut the Odet leucogranite dated at 324 ± 5 Ma (U/Pb on zircon; Cocherie, 2001). The Kerjulien Sb-As vein deposit (to the east from the Quimper district) crosscuts the Langonnet leucogranite dated at 304.7 ± 2.7 Ma (Ballouard et al., 2017; U/Pb on zircon; Fig. 14A, C). In the Châteaulin basin, the Scubériou vein crosscuts the Visean sedimentary rocks indicating a mineralization age younger than 340 Ma. In the CAD, the Semnon Sb-Au deposit is structurally controlled by a N-S shortening direction (Bouchot et al., 1997; Pochon et al., 2018). In the SAD, the Vendée (Marcoux et al., 1984) and La Bellière districts (Cheval-Garabédian et al., 2020a) show similar structural controls, with a shortening direction (Z1) striking N05-10°E. Moreover, at the Batz-sur-Mer Sb-As mine, stibnite veins crosscut the Guérande leucogranite (Fouquet, 1980) dated at 309.7 ± 1.9 Ma (Ballouard et al., 2015; U/Pb on zircon). Consequently, those

structural and relative chronology arguments, combined with our new results got from the La Lucette support that, all the Sb-Au-(W) deposits from the AM have been emplaced during the same mineralizing event at around 310-295 Ma.

These results challenge the recent works in the CAD (Pochon et al., 2018, 2019) in which a Sb-Au hydrothermal peak at ca. 360 Ma is suggested for the Semnon Sb-Au deposit. This hydrothermal event is assumed to be coeval with the regional emplacement of the dolerites, dated at ca. 363.0 ± 3.1 Ma by apatite U/Pb LA-ICP-MS method (Pochon et al., 2016). The radiometric age of the mineralization has been inferred on the basis of apatite U/Pb measurements on a hydrothermalized dolerite dyke surrounding the mineralization. Indeed, the dated apatite grains include a magmatic core surrounded by a hydrothermal rim. However, due to their small size, the age of these overgrowths is not dated. Furthermore, illite $^{40}Ar/^{39}Ar$ ages picked up directly from the Sb-Au quartz vein show disturbed saddle-shaped age spectra difficult to interpret, with a maximum age of335 Ma interpreted as postponing the main Sb-Au mineralization (Pochon et al., 2018). Consequently, we suggest that the ca 360 Ma apatite U/Pb age corresponds more likely to the dolerite dyke emplacement, such as demonstrated for other dolerite dykes in the AM (Pochon et al., 2016), rather than the Sb-Au hydrothermal event. Other arguments, namely: i) the structural features showing dolerite dykes clearly crosscut by the ore-veins, ii) the presence of hydrothermal alteration of the dolerite dykes along the ore-veins contacts, iii) the non-magmatic fluid inclusion signatures (i.e. salinity, dissolved components) and relatively low fluid temperature (between 240 to 330 °C; Pochon et al., 2018), suggest a temporal decoupling between the dolerite dyke emplacement and ore deposition. Hence a time discontinuity between magmatic and mineralizing hydrothermal fluid circulation appears as another possibility.

7.5 Ore-genesis model and comparison with other Variscan Sb-Au deposits

A possible emplacement model for the La Lucette deposit is depicted in Fig. 15. All our results show that no additional heating source, such as the late Variscan leucogranitic magmatism is needed for the genesis of the La Lucette deposit. This is consistent with the regional geological history, no late-Variscan magmatism is documented in the proximity of the La Lucette deposit (Fig. 14B). Our view challenges the previous genetic models proposed for the Sb-Au mineralizations in the AM (Chauris and Marcoux, 1994; Bouchot et al., 1997), or in the FMC (Bril and Beaufort, 1989, Marignac and Cuney, 1999; Bouchot et al., 2005). The paragenetic and FI data presented in the previous sections document the temporal and genetic disconnection between the late Devonian to early Carboniferous mafic magmatism and the Sb-Au-(W) metallogenic peak. This result is at variance with the recent works in which the heat supplied by the mafic magmatism was invoked to insure the fluid heating and the ore-fluid flow for the Sb-Au deposit in the Variscan massifs (Pochon et al., 2016, 2018, 2019).

Recent works on the actual geothermal system of the Dormant fault (Eastern Pyrénées, France; Taillefer et al., 2018) supports also our model. The authors have shown that cold meteoric water infiltration can be channeled by fault system at great depth (more than 3 km) associated with geothermal gradients of 100-160 °C/km, without any magmatism implications.

We propose that the hot aqueous-carbonic fluids involved from the early stages of the mineralization was possibly derived from regionally deep metamorphic dehydration processes. Then ore-fluid was channeled by a crustal drain such as the NASZ, towards inherited structural traps represented by pre-existing N110-120°E trending antiforms. The mineralization precipitated within voids (i.e. tension gashes) opened during faulting (Fig. 14A, 15). Such a hot CO_2 -rich fluid is chemically more favorable for tungsten solubilization and transport nd might explain its early deposition (Wood and Samson, 2000). The higher amount of N_2 and CH_4 at the early stage could indicate an important fluid/rock interaction with the surrounding black shale formations, that could be responsible for scheelite precipitation. The shallow seismic

activity on the fault zone that led to the percolation of cold meteoric fluids at depth and subsequent mixing with metamorphic fluids, could have triggered the late deposition of the economic Sb-Au ore (Fig. 15). Our model is consistent with the intense period of meteoric fluid infiltration down to the brittle/ductile transition (around 8 km depth) recorded in the major shear zone system from the AM between 320-300 Ma, coeval with the emplacement of the La Lucette and the other Sb-Au deposits (Tartèse and Boulvais 2010; Lemarchand et al., 2011; Tartèse et al., 2013; Dusséaux et al., 2019, 2022).

A comparison of the La Lucette district with other Sb-As and Sb-Au deposits, located in the AM (Serment, 1978; Fouquet, 1980; Marcoux et al., 1984 ; Chauris and Marcoux, 1994; Bouchot et al., 1997; Bailly et al., 2000; Pochon et al., 2018, 2019; Cheval-Garabédian et al., 2020a), in the FMC (Périchaud, 1980; Bril and Beaufort, 1989; Munoz et al., 1991; Bril et al., 1994; Marignac and Cuney, 1999; Bellot et al., 2003; Bouchot et al., 2005), and in the European Variscan Belt (Wagner and Cook, 2000; Bellot et al., 2003; Neiva et al., 2008; Němec and Zachariáš, 2018; Krolop et al., 2019; Epp et al., 2019) highlights a significant number of similarities. These include: i) an emplacement age during the late-orogenic processes between 310-295 Ma (Fig. 14C; see part 7.4 for the AM), although an early mineralizing peak between 345-330 Ma has been recognized in the Bohemian Massif; ii) a mineralogical evolution with three typical metal associations, with an early As-Fe, then a Fe-Zn-Cu-Pb ± Sb, and a late Sb-Au ± Pb stage; iii) a shallow depth and a cold temperature of emplacement (≤ 5 km); iv) a predominant mechanism of mixing between a metamorphic fluid and a late meteoric one enhancing ore deposition. Thus, a common genetic model with similar fluid compositions and mechanism of formation dominated by fluid cooling and mixing, can be invoked for all those Variscan districts. The similar late-Variscan deposition ages indicate that a relatively comparable ore-fluid features/source independent of the host rock, has occurred simultaneously in the entire European Variscan Belt during the late Variscan episode.

At the European Variscan Belt scale, this main Sb metallogenic peak has close spatial and temporal relationships with the late-Variscan orogenic-gold deposits ("Or300" event), as clearly illustrated in the FMC (Marignac and Cuney, 1999; Bouchot et al., 2005). Thus, this main event could be a low temperature, more surficial and another expression of the major "Or300" metallogenic peak recognized in the European Variscan Belt (Fig. 14C; Bouchot et al., 2005), and could correspond to a different expression of the "epizonal Au-Sb mineralization" in the classification of the orogenic gold deposits proposed by Groves et al. (1998). Even if the La Lucette deposit displays an uncommon W ore associated with the Sb-Au, its genetic and ore-forming fluids features could be a Variscan example of the Woxi Au-Sb-W orogenic-vein-type deposit of China (Peng et al., 2005; Zhu and Peng, 2015; Fu et al., 2020; Dai et al., 2022; Yan et al., 2022).

Conclusions

The La Lucette represents the only known example of Sb-Au-(W) deposit of France. Our study documents that the mineralization occurred during a same and continuous tectonic-hydrothermal event in response to shallow seismic activities. A first aqueous-carbonic hot fluid from a deep metamorphic source was involved in the early stages (scheelite to base-metals) with trapping temperatures around 350 to 250 °C, and an estimated emplacement depth between 6 to 5 km. An aqueous cold fluid with temperature between 200 to 133 °C and estimated shallow trapping depth between 6 to 3.5 km, is related to the deposition of the late Sb-Au stage. The general fluid-cooling trend could be explained by the mixing of the initial aqueous-carbonic hot fluid with a late cold meteoric fluid, which enhance Sb concentration in the ore-fluid.

Those P-T conditions do not involve important exhumation rates, and no additional thermal source such as from the late-Variscan leucogranitic magmatism, or the early Carboniferous mafic event are needed for the Sb-Au ore-genesis.

Our new hydrothermal apatite LA-ICP-MS U/Pb dating from the La Lucette deposit indicates an emplacement age at 299 ± 11 Ma. Coupled with other results on similar deposits, we highlight that a main major Sb-Au-(W) mineralizing peak operated at 310-295 Ma in the entire Armorican Massif. This hydrothermal event is controlled at regional scale by brittle dextral strike-slip motions coeval with a late-orogenic transpressional context.

The common features between the La Lucette and the other Sb-Au districts indicate that a relatively similar fluid source has been mobilized simultaneously in the several areas of the European Variscan Belt during the late-orogenic episode. Our results provide new guides for the mining exploration and suggests that the economic high-grade Au and W contents in Sb vein-type deposits might have been underestimated in the French Variscan massifs.

Acknowledgements.

This work was funded by e-Mines Company through its R&D activity, and the ISTO with contribution from ANRT. The authors thank the following persons for their technical support, the provision of samples, and the valuable advices: T. Poitrenaud, B. Cochelin, C. Hulin, C. Montmartin J. Gouin, M. Picault, and the team of the Museum of the Ecole-des-Mines from Paris. We particularly thank Pr. Colette Derré (Paris 6 University) for the rock samples and L. Bailly (BRGM) from its great help in IR fluid inclusion analyses and for valuable advices. I. Di Carlo (ISTO) for the SEM, cathodoluminescence and microprobe analyses and for valuable advices. S. Janiec, G. Badin, and P. Benoist-Julliot (ISTO) for thin sections preparation, and technical assistance. The GeOHeLiS platform and in particular M. Poujol for the LA-ICP-MS dating and valuable advices.

References

A'xiang, H., Jiantang, P., 2018. Fluid inclusions and ore precipitation mechanism in the giant Xikuangshan mesothermal antimony deposit, South China: conventional and infrared microthermometric constraints. Ore Geol Rev 95:49–64.

Akçay, M., Özkan, MH., Moon, CJ., Spiro, B., 2006. Geology, mineralogy and geochemistry of the gold-bearing stibnite and cinnabar deposits in the Emirli and Haliköy areas (Ödemis, Izmir, West Turkey). Ore Geol Rev 29:19–51. doi:10.1016/j.oregeorev.2004.12.006.

Allon, A., 1981. Les minéralisations à antimoine-or de Mesnard-la-Barotière - Les Brouzils (Vendée), état des connaissances au 30-10-1981. Rapp BRGM/81.RDM.060.FE, pp 106.

André-Mayer, AS., Leroy, J., Bailly, L., Chauvet, A., Marcoux, E., Grancea, L., Liosa, F., Rosas, J., 2002. Boiling and vertical mineralization zoning: a case study from the Apacheta low-sulfidation epithermal gold-silver deposit, southern Peru. Miner Deposita 37:452–464.

Audion, AS., 2012 Panorama 2011 du marché de l'antimoine. Rapp BRGM/RP-61342-FR, pp 82.

Augier, R., Choulet, F., Faure, M., Turrillot, P., 2015 A turning-point in the evolution of the Variscan orogen: The ca. 325 Ma regional partial-melting event of the coastal South Armorican domain (South Brittany and Vendée, France). Bull Soc géol Fr 186:63–91.

Bailly, L., Bouchot, V., Bény, C., Milési, J., 2000. Fluid inclusion study of stibnite using infrared microscopy: an example from the Brouzils antimony deposit (Vendée, Armorican Massif, France). Econ Geol 95:221–226.

Bakker, RJ., 1999. Adaptation of the Bowers and Helgeson (1983) equation of state to the H2O-CO2-CH4-N2-NaCl system. Chem Geol 154:225–236.

Bakker, RJ., 2003. F.L.U.I.D.S. Package 1, Computer programs for analysis of fluid inclusion data and for modelling bulk fluid properties. Chem Geol 194:3–23.

Ballèvre, M., Bosse, V., Ducassou, C., Pitra, P., 2009. Palaeozoic history of the Armorican Massif: Models for the tectonic evolution of the suture zones, Comptes Rendus Geosci, pp 28.

Ballouard, C., Boulvais, P., Poujol, M., Gapais, D., Yamato, P., Tartese, R., Cuney, M., 2015. Tectonic record, magmatic history and hydrothermal alteration in the Hercynian Guérande leucogranite, Armorican Massif, France. Lithos 220:1–22.

Ballouard, C., Poujol, M., Boulvais, P., Zeh, A., 2017. Crustal recycling and juvenile addition during lithospheric wrenching: The Pontivy-Rostrenen magmatic complex, Armorican Massif (France), Variscan belt. Gondwana Research, 49:222–247.

Ballouard, C., Poujol, M., Mercadier, J., Deloule, E., Boulvais, P., Baele, JM., Cuney, M., Cathelineau, M., 2018. Uranium metallogenesis of the peraluminous leucogranite from the Pontivy-Rostrenen magmatic complex (French Armorican Variscan belt): the result of long-term oxidized hydrothermal alteration during strike-slip deformation. Mineral Deposita 53:601–628.

Bastit, G., 1930. Renseignements géologiques sur le gisement de La Lucette. Rapp. Inédit de Soc. Nouv. Min. Lucette.

Bellanger, H., 1921. Le filon Georges des mines de La Lucette. Ann. Mines, t. XII, pp 83–117.

Bellot, JP., Lerouge, C., Bailly, L., Bouchot, V., 2003. The Biards Sb-Au–Bearing Shear Zone (Massif Central, France): An Indicator of Crustal-Scale Transcurrent Tectonics Guiding Late Variscan Collapse. Econ Geol 98:1427–1447. doi:10.2113/gsecongeo.98.7.1427.

Berthé, D., Choukroune, P., Jegouzo, P., 1979. Orthogneiss, mylonite and non-coaxial deformation of granites: the example of the South Armorican Shear Zone. Journal of Structural Geology 1:31–42.

Bodnar, R.J., 1993. Revised equation and table for determining the freezing-point depression of H 2 O–NaCl solutions. Geochim Cosmochim Acta 57:683–684.

Boiron, M.C., Cathelineau, M., Trescases, J.J., 1989. Conditions of gold-bearing arsenopyrite crystallization in the Villeranges Basin, Marche-Combrailles shear zone, France; a mineralogical and fluid inclusion study. Econ Geol 84:1340–1362.

Boiron, M.C., Cathelineau, M., Dubessy, J., Bastoul, A.M., 1990. Fluids in Hercynian Au veins from the French Variscan belt. Mineralogical Mag 54:231–243.

Boiron, M.C., Cathelineau, M., Banks, D.A., Fourcade, S., Vallance, J., 2003. Mixing of metamorphic and surficial fluids during the uplift of the Hercynian upper crust: consequences for gold deposition. Chem Geol 194:119–141.

Bonjour, J.L., 1988. Conséquences stratigraphiques des premières données radiométriques concernant l'âge de la transgression paléozoïque en Bretagne centrale. C. R. Acad. Sci., Paris, 307:1651–1654.

Bons, P.D., Elburg, M.A., Gomez-Rivas, E., 2012. A review of the formation of tectonic veins and their microstructures. Journal of Structural Geology, 43:33–62.

Bouchot, V., Gros, Y., Piantone, P., 1994. Dynamics of shallow late-Variscan gold mineralization: the Le Châtelet Au-arsenopyrite quartz veins, Massif Central, France. Miner Deposita 29: 461–473.

Bouchot, V., Milési, J.P., Lescuyer, J.L., Ledru, P., 1997. Les minéralisations aurifères de la France dans leur cadre géologique autour de 300 Ma: Chron Rech min 528: 13–62.

Bouchot, V., Ledru, P., Lerouge, C., Lescuyer, J.L., Milesi, J.P., 2005. Late Variscan mineralizing systems related to orogenic processes: the French Massif Central. Ore Geol Rev 27:169–197.

Bril, H., Beaufort, D., 1989. Hydrothermal alteration and fluid circulation related to W, Au, and Sb vein mineralizations, Haut-Allier, Massif Central, France: Econ Geol 84:2237–2251.

Bril, H., Bonhomme, M.G., Marcoux, E., Baubron, J.C., 1991. Ages K/Ar des minéralisations de Brioude-Massiac (W-Au-As-Sb; Pb-Zn), Pontgibaud (Pb-Ag; Sn), et Labessette (As-Pb-Sb-Au): Place de ces districts dans l'évolution géotectonique du Massif Central français: Miner Deposita 26:189–198.

Bril, H., Marignac, Ch., Cathelineau, M., Tollon, F., Cuney, M., Boiron, M.C., 1994. Metallogenesis of the French Massif Central: Time-space relationships between ore deposition and tectono-magmatic events. Pre-Mesozoic Geology in France and Related Areas, part III, 379–402.

Chantraine, J., Atran, A., Cavelier, C., 1996. Geological map of France, 1/1 000 000. BRGM, Orléans.

Chauris, L., Marcoux, E., 1994. Metallogeny of the Armorican Massif. Pre-Mesozoic Geology in France and Related Areas, pp 22.

Chauvet, A., Bailly, L., André-Mayer, A.S., Monié, P., Cassar, D., Liosa Tajada, F., Vargas, J.R., Tuduri, Y., 2006. Internal vein texture and vein evolution of the epithermal Shila-Paula district, southern Peru. Miner Deposita 41:387–410.

Chauvet, A., Volland-Tuduri, N., Lerouge, C., Bouchot, V., Monié, P., Charonnat, X., Faure, M., 2012. Geochronological and geochemical characterization of magmatic-hydrothermal events within the Southern Variscan external domain (Cévennes area, France). Int J Earth Sci. 101:69–86. DOI 10.1007/s00531-011-0639-1.

Cheval-Garabédian, F., 2019. Les minéralisations à Sb et Au tardi-varisques : vers un modèle génétique unifié ? Exemples du Massif armoricain et du Massif central, PhD thesis, Université d'Orléans, 1 Vol, pp 498.

Cheval-Garabédian, F., Faure, M., Marcoux, E., Gouin, J., Picault, M., 2020a. The La Bellière gold and antimony district (French Armorican Massif): A two-stage evolution model controlled by Variscan strike-slip tectonic. Ore Geol Rev 125:103–681.

Cheval-Garabédian, F., Faure, M., Marcoux, E., Poujol, M., 2020b. The tungsten-gold veins of Bonnac (French Massif central): new constraints for a Variscan granite-related genesis. Bull Soc Géol France. https://doi.org/10.1051/bsgf/2020041.

Chew, DM., Petrus, J.A., Kamber, B.S., 2014. U-Pb LA–ICPMS dating using accessory mineral standards with variable common Pb. Chem Geol 363:185–199.

Chovan, M., Hurai, V., Sachan, H.K., Kantor, J., 1995. Origin of the fluids associated with granodiorite-hosted, Sb–As–Au–W mineralisation at the Dubrava (Nızke-Tatry Mts., Western Carpathians). Miner Deposita 30:48–54.

Chovan, M., Majzlan, J., Ragan, M., Siman, P., Kristin, J., 1998. Pb-Sb and Pb-Sb-Bi sulfosalts and associated sulphides from Dubrava antimony deposit, Nizke Tatry Mts: Acta Geologica Universitatis Comenianae 53:37–49.

Cocherie, A., 2001. Datations à la SHRIMP II dans le cadre du projet carte 1/50 000 des zircons magmatiques de l'Orthogneiss du Loc'h et du Granite d'Odet. Rapport interne BRGM AC/02.01, pp 8.

Cocherie, A., 2007. Datations U-Pb (laser-ICPMS-MC) sur zircons et U-Th-Pb sur monazites de granitoïdes du Pertre (carte de Cossé-le-Vivien). Rapport d'essais BRGM : 2007/281, pp 23.

Collins, P.L.F., 1979. Gas hydrate in CO2 -bearing fluid inclusions and the use of freezing data for estimation of salinity – Econ Geol 74:1435–1444.

Couto, H., Roger, G., Moelo, Y., Bril, H., 1990. Le district à antimoine-or Durico-Beirao (Portugal): évolution paragenétique et géochimique; implications métallogéniques. Miner Deposita 25:69–81.

Dai, J., Xu, D., Chi, G., Li, Z., Deng, T., Zhang, J., Li, B., 2022. Origin of the Woxi Orogenic Au-Sb-W Deposit in the West Jiangnan Orogen of South China: Constraints from Apatite and Wolframite U-Pb Dating and Pyrite in-situ S-Pb Isotopic Signatures, Ore Geology Reviews; doi: https://doi.org/10.1016/j.oregeorev.2022.105134.

Dill, H.G., 1985. Antimoniferous mineralization from the Mid-European Saxothuringian zone: mineralogy, geology, geochemistry and ensialic origin. Geol Rundsch 74:447–466

Dill, H.G., Melcher, F., Botz, R., 2008. Meso- to epithermal W-bearing Sb vein-type deposits in calcareous rocks in western Thailand; with special reference to their metallogenetic position in SE Asia. Ore Geol Rev 34:242–262.

Dong, G., Morrison, G., Jaireth, S., 1995. Quartz textures in epithermal veins, queensland-classification, origin and implication. Econ Geol 90:1841–1856.

Douxami, H., 1907. Les minerais de La Lucette, près du Genest (Mayenne). Liégeois-Six impr. Lille.

Dowling, K., Morison, G., 1988. Application of quartz textures to the classification of gold deposits using North Queensland examples. Econ. Geol. Monograph 6:342–355.

Dusséaux, C., Gébelin, A., Boulvais, P., Gardien, V., Grimes, S., Mulch, A., 2019. Meteoric fluid-rock interaction in Variscan shear zones. Terra Nova 31 :366 –372.

Dusséaux, C., Gébelin, A., Boulvais, P., Ruffet, G., Poujol, M., Cogné, N., Branquet, Y., Mott ram, C., Barou, F., Mulch, A., 2022. Timing and duration of meteoric water infiltrati on in the Quiberon detachment zone (Armorican Massif, Variscan belt, France). Journal of Structural Geology, 156.

Epp, T., Walter, B., Scharrer, M., Lehmann, G., Henze, K., Heimgärtner, C., Bach, W., Markl, G., 2019. Quartz veins with associated Sb-Pb-Ag±Au mineralization in the Schwarzwald, SW Germany: a record of metamorphic cooling, tectonic rifting, and element remobilization processes in the Variscan belt. Mineral Deposita 54:281–306.

Faure, M., Be Mézème, E., Duguet, M., Cartier, C., Talbot, J.Y., 2005. Paleozoic tectonic evolution of medio-Europa from the example of the French Massif Central and Massif Armorican. In: (eds.) Carosi, R., Dias, R., Iacopini, D., and Rosenbaum, G., The southern Variscan belt, Journal of the Virtual Explorer, Electronic Edition, ISSN 19:1441–8142.

Faure, M., Bé Mézème, E., Cocherie, A., Rossi, P., Chemenda, A., Boutelier, D., 2008. Devonian geodynamic evolution of the Variscan Belt, insights from the French Massif Central and Massif Armorican, Tectonics 27:1–19.

Fouquet, M., 1980. Les districts antimonifères de Quimper et du Cap Sizun (Finistere) leur place dans la métallogénie de I'antimoine dans le Massif Armoricain (France), Thése, Clermont-Ferrand, pp 212.

Fu, S., Lan, Q., Yan, J., 2020. Trace element chemistry of hydrothermal quartz and its genetic significance: A case study from the Xikuangshan and Woxi giant Sb deposits in southern China. Ore Geol Rev, 126:103732.

Goldstein, R.H., Reynolds, T.J., 1994. Systematics of fluid inclusions in diagenetic minerals: Society for Sedimentary Geology Short Course 31, pp 199.

Graviou, P., Peucat, J.J., Auvray, B., Vidal, P., 1988. The Cadomian Orogeny in the northern Armorican Massif: petrological and geochronological constraints on a geodynamic model. Hercynica 1:1–13.

Groves, D.I., Goldfarb, R.J., Gebre-Mariam, M., Hagemann, S.G., Robert, F., 1998. Orogenic gold deposits, a proposed classification in the context of their crustal distribution and relationship to other gold deposit types. Ore Geol Rev 13:7–27.

Guerrot, C., Calvez, J.Y., Bonjour, J.L., Chantraine, J., Chauvel, J.J., Dupret, L., Rabu, D., 1992. Le Briovérien de Bretagne centrale et occidentale : nouvelles données radiométriques. Comptes Rendus de l'Académie des Sciences de Paris, 315:1741–1746.

Guiollard, P.C., 1995. La mine d'or et d'antimoine de La Lucette (Mayenne). Ed. P. C. Guiollard, pp 120.

Gumiaux, C., Gapais, D., Brun, J.P., Chantraine, J., Ruffet, G., 2004. Tectonic history of the Hercynian Armorican Shear belt (Brittany, France). Geodinamica Acta, Vol. 17:289–307.

Gumiel, P., Arribas, A., 1987. Antimony deposits in the Iberian Peninsula. Econ Geol 82:1453–1463.

Harlaux, M., Romer, R.L., Mercadier, J., Morlot, C., Marignac, C., Cuney, M., 2018. 40 Ma of hydrothermal W mineralization during the Variscan orogenic evolution of the French Massif Central revealed by U-Pb dating of wolframite. Miner Deposita 53:21–51.

Houlgatte, E., Le Herisse, A., Pelhate, A., Rolet, J., 1988. Evolution géodynamique du bassin carbonifère de Laval (Massif Armoricain). Géologie de la France 1:27–46.

Jébrak, M., 1985. Contribution à l'histoire naturelle des filons (F, Ba) du domaine varisque. PhD thesis, BRGM, Université d'Orléans, 1 Vol, pp 473.

Jébrak, M., 1992. Les textures intra-filoniennes, marqueurs des conditions hydrauliques et tectoniques : Chron Rech min 506:55–65.

Jébrak, M., 1997. Hydrothermal breccias in vein-type ore deposits: a review of mechanisms, morphology and size distribution. Ore geol Rev 12:111–134.

Jégouzo, P., 1980. The South Armorican shear zone, J. of Struct. Geol. 2, pp 39.

Jégouzo, P., Rossello, A.E., 1988. The northern branch of the South Armorican Shear Zone (France) - An attempt to evaluate the displacement magnitude from analysis of mylonites. Comptes Rendus de l'Académie des Sciences 307:1825–1831.

Kontak, D.J., Horne, R.J., Smith, P.K., 1996. Hydrothermal characterization of the West Gore Sb-Au deposit, Meguma Terrane, Nova Scotia, Canada. Econ Geol 91:1239–1262.

Kornyenko, P., 1960. Fiche de gîte à antimoine de Batz-sur-Mer. Fiche d'inventaire BRGM national BSS n°479-1X-4002, pp 8.

Kretschmar, U., Scott, S.D., 1976. Phase relations involving arsenopyrite in the system Fe-As-S and their application: The Canadian Mineralogist 14:364–386.

Krolop, P., Burisch, M., Richter, L., Fritzke, B., Seifert, T., 2019. Antimoniferous vein-type mineralization of the Berga Antiform, Eastern-Thuringia, Germany: A fluid inclusion study. Chem Geol, 508:47–61.

Le Gall, J., 1993. Reconstitution des dynamismes éruptifs d'une province paléovolcanique : l'exemple du graben cambrien du Maine (Est du Massif armoricain). Pétrogenèse des magmas andésitiques et ignimbritiques et leur signification dans l'évolution géodynamique cadomienne. Thèse Université de Caen, pp 370.

Le Gall, J., Gigot, P., Savaton, P., Lacquement, F., Poprawsky, Y., Vernhet, Y., 2011. Carte géologique de la France (1/50000), feuille Laval (319), BRGM, Orléans.

Lemarchand, J., Boulvais, P., Gaboriau, M., Boiron, M.C., Tartèse, R., Cokkinos, M., Bonnet, S., Jégouzo, P., 2011. Giant quartz vein formation and high-elevation meteoric fluid infiltration into the South Armorican Shear Zone: geological, fluid inclusion and stable isotope evidence. Journal of the Geological Society, London, 168:1–11.

Lescuyer, J.L., Leistel, J.M., Marcoux, E., Milési, J.P., Thiéblemont, D., 1997. Late Devonian-Early Carboniferous peak sulphide mineralization in the Western Hercynides. Miner Deposita 33:208–220.

Lüders, V., 1996. Contribution of infrared microscopy to fluid inclusion studies in some opaque minerals (wolframite, stibnite, bournonite): metallogenic implications. Econ Geol 91:1462–1468.

Machairas, G., 1974 Présence de gersdorffite, chalcostibite et zinkénite dans la minéralisation de La Lucette. Rapport BRGM MET/GIT-304, BRGM, Orléans.

Marcoux, E., Serment, R., Allon, A., 1984. Les gites d'antimoine de Vendée (Massif Armoricain, France Historique des recherches et synthèses métallogénique, Chron Rech min 476:3–30.

Marignac, C., Cuney, M., 1999. Ore deposits of the French Massif Central: insight into the metallogenesis of the Variscan collision belt. Miner Deposita 34:472–504.

Matte, P., 1986. La chaîne Varisque parmi les chaînes Paléozoïques péri atlantiques modèle d'évolution et position des grands blocs continentaux au Permo-Carbonifère, Bull. Soc. géol. Fr. 2:9–24.

McDowell, F.W., McIntosh, W.C., Farley, K.A., 2005. A precise 40Ar–39Ar reference age for the Durango apatite (U–Th)/He and fission-track dating standard. Chem Geol 214:249–263.

Moritz, R., 2006. Fluid salinities obtained by infrared microthennometry of opaque minerals: implications for ore deposit modeling. A note of caution. J Geochem Explor 89:284–287.

Munoz, M., Shepherd, T.J., 1987. Fluid inclusion study of the Bournac polymetallic (Sb-As-Pb-Zn-Fe-Cu…) vein deposit (Montagne Noire, France). Miner Deposita 22:11–17.

Munoz, M., Courjault-Radé, P., Tollon, F., 1991. The massive stibnite veins of the French Palaeozoic basement: A metallogenic marker of late Variscan brittle extension: Terra Nova 4:171–177.

Neiva, A.M.R., Andras, P., Ramos, J.M.F., 2008. Antimony quartz and antimony-gold quartz vein from northern Portugal. Ore Geol Rev 34:533–546.

Němec, M., Zachariáš, J., 2018. The Krásná Hora, Milešov, and Příčovy Sb-Au ore deposits, Bohemian Massif: mineralogy, fluid inclusions, and stable isotope constraints on the deposit formation. Miner Deposita 53:225–244.

Nicaud, J., 2001. Contrôle structural de la mise en place des minéralisations aurifères du district de Saint-Yrieix : analyse de la fracturation, étude des altérations hydrothermales. Thèse, Université de Limoges, pp 252.

Obolensky, A.A., Gushchina, L.V., Borisenko, A.S., Borovikov, A.A., Nevolko, P.A., 2009. Computer thermodynamic modeling of the transport and deposition of Sb and Au during the formation of Au-Sb deposits. Russian Geology and Geophysics 50:950–965.

Paquette, J.L., Piro, J.L., Devidal, J.L., Bosse, V., Didier, A., Sanac, S., Abdelnour, Y., 2014. Sensitivity enhancement in LA-ICP-MS by N2 addition to carrier gas: Application to radiometric dating of U-Th-bearing minerals. Agilent ICP-MS J 58:4–5.

Pasteels, A., Doré, F., 1982. Age of the Vire-Carolles granites. In G.S. Odin (ed.): «Numerical dating in stratigraphy », pp 784-790.

Paton, C., Woodhead, J.D., Hellstrom, J.C., Hergt, J.M., Greig, A., Maas, R., 2010. Improved laser ablation U-Pb zircon geochronology through robust downhole fractionation correction. Geochem Geophys Geosyst 11 Q0AA06.

Peng, J.T., Hu, R.Z., Zhao, J.H., Fu, Y.Z., Yuan, S.D., 2005. Rare earth element (REE) geochemistry for scheelite from the Woxi Au–Sb–W deposit, western Hunan. Geochimica 34:115–122.

Périchaud, J.J., 1980. L'antimoine, ses minerais et ses gisements. Synthèse gîtologique sur les gisements du Massif Central français. Chron Rech min 456:5–64.

Pierrot, R., Chauris, L., Laforet, C., 1975. Inventaire minéralogique de la France (Côtes-du-Nord), 5. Orléans: BRGM, pp 220.

Pitra, P., Ballèvre, M., Ruffet, G., 2010. Inverted metamorphic field gradient towards a Variscan suture zone (Champtoceaux Complex, Armorican Massif, France). J. metamorphic Geol. 28, 183–208

Pochon, A., 2017. Magmatisme mafique et minéralisations à Sb-Au dans le domain Centre Armoricain : contrôles spatio-temporels et implications métallogéniques. Thèse, Université de Rennes, pp 334.

Pochon, A., Gapais, D., Gloaguen, E., Gumiaux, C., Branquet, Y., Cagnard, F., Martelet, G., 2016. Antimony deposits in the Variscan Armorican belt, a link with mafic intrusives ? Terra Nova 28:138–145. doi: 10.1111/ter.12201.

Pochon, A., Gloaguen, E., Branquet, Y., Poujol, M., Ruffet, G., Boiron, M.C., Boulvais, P., Gumiaux, C., Cagnard, F., Gouazou, F., Gapais, D., 2018. Variscan Sb-Au mineralization in Central Brittany (France): A new metallogenic model derived from the Le Semnon district. Ore Geol Rev 97:109–142.

Pochon, A., Branquet, Y., Gloaguen, E., Ruffet, G., Poujol, M., Boulvais, P., Gumiaux, C., Cagnard, F., Baele, J.M., Kéré, I., Gapais, D., 2019. A Sb±Au mineralizing peak at 360 Ma in the Variscan belt. BSGF-Earth Sciences Bulletin, 190, 4.

Poitrenaud, T., 2018. Le gisement périgranitique à tungstène et or de Salau (Pyrénées, France), histoire polyphasée d'un système minéralisé tardi-varisque. Thèse, Université d'Orléans, pp 490.

Rolin, P., Colchen, M., 2001. Les cisaillements hercyniens de la Vendée au Limousin. Géologie Fr. 1:87–116.

Schoene, B., Bowring, S.A., 2006. U-Pb systematics of the McClure Mountain syenite: thermochronological constraints on the age of the 40Ar/39Ar standard MMhb. Contrib. Mineral. Petrol. 151:615–630.

Scholz, C.H., 1988. The brittle-plastic transition and the depth of seismic faulting. Geologische Rundschau 77:319–328.

Schwarz-Schampera, U., 2014. Antimony. In: Gunn, G. (Ed): Critical Metals Handbook, American Geophysical Union - John Wiley & Sons, Ltd, pp 70–98.

Seal, R.R., Robie, R.A., Barton, P.B., Hemingway, B.S., 1992. Superambient heat capacities of synthetic stibnite, berthierite, and chalcostibnite: Revised thermodynamic properties and implications for phase equilibria: Econ Geol 87:1911–1918.

Serment, R., 1978. La mine d'antimoine et or de La Lucette (Mayenne, France), Chron Rech min 442:35–42.

Sharp, Z.D., Essene, E.J., Kelly, W.C., 1985. A re-examination of the arsenopyrite geothermometer; pressure considerations and applications to natural assemblages. Can Mineral 23:517–534.

Sibson, R.H., 1987. Earthquake rupturing as a hydrothermal mineralizing agent. Geology 15: 701–704.

Simmons, S.F., White, C.N., John, D.A., 2005. Geological characteristics of Epithermal precious and base metal deposits. Economic Geology 100th Anniversary, pp 485–522.

Taillefer, A., Guillou-Frottier, L., Soliva, R., Magri, F., Lopez, S., Courrioux, G., Millot, R., Ladouche, B., Le Goff, E., 2018. Topographic and faults control of hydrothermal circulation along dormant faults in an orogen. Geochemistry, Geophysics, Geosystems, 19(12), 4972-4995.

Tartèse, R., Boulvais, P., 2010. Differentiation of peraluminous leucogranites "en route" to the surface. Lithos, 114, 353–368.

Tartèse, R., Poujol, M., Ruffet, G., Boulvais, P., Yamato, P., Košler, J., 2011. New U-Pb zircon and 40Ar/39Ar muscovite age constraints on the emplacement of the Lizio syn-tectonic granite (Armorican Massif, France). Comptes Rendus Geosci 343:443–453.

Tartèse, R., Boulvais, P., Poujol, M., Gloaguen, E., Cuney, M., 2013. Uranium Mobilization from the Variscan Questembert Syntectonic Granite During Fluid-Rock Interaction at Depth. Economic Geology, 108, 379–386.

Thomson, S.N., Gehrels, G.E., Ruiz, J., Buchwaldt, R., 2012. Routine low-damage apatite U-Pb dating using laser ablation–multicollector–ICPMS. Geochem Geophys Geosyst 13 Q0AA21.

Vasquez Lopez, R., Blouin, J.P., 1991. Gisement d'antimoine des Brouzils point des travaux et actualisation des réserves à fin décembre 1990. Rapp BRGM DAM/DL/Nantes RVL/FD 91-01, pp 35.

Vermeesch, P., 2018. IsoplotR: A free and open toolbox for geochronology. Geosci. Front. 9:1479–1493. https://doi.org/10.1016/J.GSF.2018.04.001.

Vernhet, Y., Plaine, J., Trautmann, F., Pivette, B., Chèvremont, P., Bourdillon, C., Cocherie, A., 2009. Notice explicative, Carte géol. France (1/50 000), feuille Cossé-le-Vivien (355). Orléans : BRGM, pp 222.

Wagner, T., Cook, N.J., 2000. Late-Variscan antimony mineralisation in the Rheinisches Schiefergebirge, NW Germany: Evidence for stibnite precipitation by drastic cooling of high-temperature fluid systems. Miner Deposita 35:206–222.

Walter, B.F., Burisch, M., Fusswinkel, T., Marks, M.A.W., Steele-MacInnis, M., Wälle, M., Apukhtina, O.B., Markl, G., 2018. Multi-reservoir fluid mixing processes in rift-related hydrothermal veins, Schwarzwald, SW-Germany. J Geochem Explor 186:158–186.

Watts, M.J., Williams, G.D., 1979. Fault rocks as indicators of progressive shear deformation in the Guingamp region, Brittany. J. Struct. Geol. 1:323–332.

Wei, W.F., Hu, R.Z., Bi, X.W., Peng, J.T., Su, W.C., Song, S.Q., Shi, S.H., 2012. Infrared microthermometric and stable isotopic study of fluid inclusions in wolframite at the Xihuashan tungsten deposit, Jiangxi province, China. Miner Deposita 47:589–605.

White, N.C., Hedenquist, J.W., 1990. Epithermal environments and styles of mineralization: Variations and their causes, and guidelines for exploration: Journal of Geochemical Exploration 36:445–474.

Whitney, D.L., Evans, B.W., 2010. Abbreviations for names of rock-forming minerals. American mineralogist, 95(1), 185-187.

Williams-Jones, A.E., Normand, C., 1997. Controls of mineral parageneses in the System Fe-Sb-S-O. Econ Geol 92:308–324.

Wood, S.A., Samson, I.M., 2000. The Hydrothermal Geochemistry of Tungsten in Granitoid Environments: I. Relative Solubilities of Ferberite and Scheelite as a Function of T, P, pH, and mNaCl. Econ Geol 95:143–182.

Wu, X., Delbove, F., Touray, J.C., 1990. Conditions of formation of gold-bearing arsenopyrite: a comparison of synthetic crystals with samples from Le Chatelet gold deposit, Creuse, France. Miner deposita 25:S8–S12.

Wyns, R., 1984. Etude géologique du champ filonien de la Bellière dans le périmètre du P.E.R de Gesté. Rapp. BRGM 84 SGN 221 GEO, Orléans, pp 70.

Yan, J., Fu, S., Liu, S., Wei, L., Wang, T., 2022. Giant Sb metallogenic belt in South China: A product of Late Mesozoic flat-slab subduction of paleo-Pacific plate. Ore Geol Rev 142:104697. https://doi.org/10.1016/j.oregeorev.2022.104697.

Zachariáš, J., Stein, H., 2001. Re–Os ages of Variscan hydrothermal gold mineralizations, Central Bohemian metallogenetic zone. In: Piestrzyński A et al. (eds) Mineral Deposits at the Beginning of the 21st Century. Swets & Zeitlinger Publishers Lisse, pp 851–854.

Zachariáš, J., Pertold, Z., Pudilová, M., Žák, K., Pertoldová, J., Stein, H., Markey, R., 2001. Geology and genesis of Variscan porphyry-style gold mineralization, Petráčkova hora deposit, Bohemian Massif. Czech Republic. Miner Deposita 36:517–541.

Zachariáš, J., Frýda, J., Paterová, B., Mihaljevič, M., 2004. Arsenopyrite and As-bearing pyrite from the Roudný deposit, Bohemian Massif. Mineral. Mag. 68:31–46.

Zachariáš, J., Paterová, B., Pudilová, M., 2009. Mineralogy, Fluid Inclusion, and Stable Isotope Constraints on the Genesis of the Roudny Au-Ag Deposit, Bohemian Massif. Econ Geol 104:3–72.

Zachariáš, J., Žák, K., Pudilová, M., Snee, L.W., 2013. Multiple fluid sources/pathways and severe thermal gradients during formation of the Jílové orogenic gold deposit, Bohemian Massif, Czech Republic. Ore Geol Rev 54:81–109.

Zhang, Y.G., Frantz, J.D., 1987. Determination of the homogenization temperatures and densities of supercritical fluids in the system NaCl-KCl-CaCl2-H2O using synthetic fluid inclusions. Chem Geol 64:335–350.

Zheng, Y., Zhang, G., Wu, Y., Yu, P., Chen, X., Hu, Z., 2022. Triassic multistage antimony-gold mineralization in the Precambrian sedimentary rocks of South China: Insights from structural analysis, paragenesis, 40Ar/39Ar age, in-situ S-Pb isotope and trace elements of the Longwangjiang-Jiangdongwan orefield, Xuefengshan Mountain. Ore Geol Rev 148:105030.

Zhu, Y.N., Peng, J.T., 2015. Infrared microthermometric and noble gas isotope study of fluid inclusions in ore minerals at the Woxi orogenic Au–Sb–W deposit, western Hunan, South China. Ore Geol Rev 65:55–69.

Figures captions

Fig. 1. Simplified geological map of the Armorican Massif (modified from Chantraine et al., 1996) with the location of Sb and Au occurrences and deposits (modified from Chauris and Marcoux, 1994). NASZ: North-Armorican Shear Zone; SASZ (N) and SASZ (S): northern and southern branches of the South-Armorican Shear Zone, respectively; NSEF: Nort-sur-Erdre Fault; A: Lopérec district; B: Quimper district; C: La Lucette district; D: Le Semnon district; E: La Bellière district; F: Vendée district. Sb: stibnite; Au: gold; Cin: cinnabar; Gn: galena; Sp; sphalerite.

Fig. 2. Geological and structural map of the western domain of the Laval basin with location of the study area (Fig. 3) and the main Sb-Au deposits and occurrences. Modified after Le Gall et al. (2011). The Pertre leucogranite is dated by the zircon U/Pb LA-ICP-MS method (Cocherie, 2007; Vernhet et al., 2009). The doleritic dykes are dated by the apatite U/Pb LA-ICP-MS method (Pochon et al., 2016).

Fig. 3. (A) Geological map of the La Lucette district showing the main Sb-Au quartz-veins modified from Guiollard (1995). (B) Mining plan of the La Lucette deposit at the -33 level with the location of the exploited mineralized quartz veins (modified from Serment, 1978). C) Interpreted cross-sections across the La Lucette deposit showing the geometry of the Sb-Au-

bearing quartz veins in the Misedon anticline (modified from Serment, 1978), after the mining plans of Bastit (1930). See figure B for the localization of the cross sections.

Fig. 4. Representative hand samples of the La Lucette ores. (A) Ore sample showing the structure of the typical Sb-Au-(W)-bearing quartz vein, from the hanging wall to the core of the vein. Early quartz generation (Qz1), late quartz (Qz2). (B) High-grade gold ore sample in close association with stibnite, beared by a cataclased early quartz generation (Qz1). Note the brecciated clasts of Late Silurian black shale country-rock. (C) High-grade stibnite ore sample observed in natural light with fractured scheelite crystals in a stibnite matrix. Note the syntaxial infilling of the vein with the brecciated facies surrounding a high-grade stibnite quartz vein core. (D) The same ore-sample as in C observed in UV light (254 nm) revealing fractured scheelite crystals cemented by a massive stibnite infilling.

Fig. 5. Microphotographs of the mineralogy of the stages 1 and 2 of the La Lucette deposit. Mineral abbreviations come from Whitney and Evans (2010). (A) Coarse scheelite (Sch) in a macrocrystalline and euhedral quartz generation (Qz1) fractured and cemented by carbonates (Carb). Pyrite (Py) is associated with host-rock clasts. (B) Same view as (A) observed in transmitted light with detailed relationships between scheelite (Sch) and macrocrystalline and euhedral quartz (Qz1) displaying fluid inclusions-rich growth bands. (C) SEM image of coarse brecciated hydrothermal apatite (Ap) crosscutting the scheelite (Sch). Some scheelite fragments are included in the apatite crystal. (D) Scheelite crystal (Sch) with macrocrystalline and euhedral quartz (Qz1). The scheelite and the Qz1 are both fractured and cemented by a microcrystalline quartz (Qz2). The Qz2 locally display fibrous texture. (E) Microcrystalline quartz infilled (Qz2) with rhombic arsenopyrite (Asp) surrounded by euhedral and dark-hyaline quartz (Qz3). QZ3 and Asp are infilled by massive stibnite (Sb) and euhedral carbonates (Carb). (F) Rhombic or rod-like habitus arsenopyrite (Asp) closely associated with sub-euhedral pyrite (Py). Both are highly brecciated and cemented by massive stibnite (Sb).

Fig. 6. Microphotographs of the stage 3, of the La Lucette deposit. (A) Sphalerite (Sp) with dendritic or rounded shapes in the euhedral and dark-hyaline quartz (Qz3), with arsenopyrite (Asp) and chalcostibite (CcSb). (B) Chalcostibite (CcSb) with sphalerite (Sp) inclusions with a rounded shapes and fractured arsenopyrite (Asp) in a euhedral and dark-hyaline quartz (Qz3). (C) SEM image of the sphalerite (Sp) with arsenopyrite (Asp), chalcostibite (CcSb) and zinkenite (Zink) assemblage. (D) Sphalerite (Sp) with chalcopyrite (Ccp), gold (Au) and stibnite (Sb) inclusions. The sphalerite is surrounded by arsenopyrite (Asp).

Fig. 7. Microphotographs of ore assemblage from the stage 4 of the La Lucette deposit. (A) Cathodoluminescence view of a euhedral and dark-hyaline quartz (Qz3) crystal in the massive stibnite (Sb). The core corresponds to a fractured and corroded Qz3 surrounded by a darker overgrowth of a new generation of hyaline quartz (Qz4), directly in contact with the stibnite. (B) Coarse scheelite (Sch) fractured and cemented by the massive stibnite (Sb) and carbonates (Carb) assemblage. Country-rock clast (Enc). (C) Detail of a fractured scheelite crystal (Sch) crosscut by the euhedral carbonates (Carb) and stibnite (Sb) in intergrowth. Pyrite (Py). (D) Stibnite (Sb) with ovoidal gold (Au) inclusions. (E) Dendritic gold (Au) in stibnite (Sb). (F) Gold (Au), stibnite (Sb) and aurostibite (Ausb) assemblage in quartz gangue.

Fig. 8. Paragenetic succession of the La Lucette Sb-Au-(W) deposit. See text for details.

Fig. 9. (A) and (B) BSE images of some dated hydrothermal apatite grains (Ap) from La Lucette deposit. Scheelite (Sch), quartz (Qz), carbonates (Carb), country-rock clasts (Enc), pyrite (Py). C) Tera-Wasserburg concordia diagrams for the hydrothermal apatite from La Lucette. n corresponds to the number of apatite grains analyzed. Ellipses and errors are reported at 2σ.

Fig. 10. Typology and petrography of the fluid-inclusions at room temperature in different gangue minerals and in the stibnite from the La Lucette deposit. (A) Fluid-inclusions of the stage 1, trapped in the macrocrystalline and euhedral quartz (Qz1), and in the scheelite (Sch),

and localization of the following views. (B) Detail of secondaries aqueous two-phases fluid-inclusions (L_{H2O}-V_{H20}) with various volatile contents and monophased liquid-rich aqueous inclusions (L_{H2O}) in scheelite (Sch). (C) Detail of primary aqueous-carbonic two-phases fluid-inclusions (L_{H2O}-L_{C02}) in the macrocrystalline and euhedral quartz (Qz1). (D) Fluid-inclusions of the stage 3, in the euhedral and dark-hyaline quartz (Qz3A) corresponding to the core to the border of the quartz crystal (Qz3B) surrounded by stibnite (Sb), and localization of the following views. (E) Group of primary aqueous-carbonic two-phases fluid-inclusions (L_{H2O}-L_{C02}) in the Qz3A. (F) Primary aqueous-carbonic three-phases fluid-inclusions (L_{H2O}-L_{CO2}-V_{C02}) contemporaneous with two-phases aqueous-carbonic fluid inclusions (L_{H2O}-L_{C02}), in the Qz3A. (G) Primary and pseudosecondary aqueous-carbonic two-phases fluid-inclusions (L_{H2O}-L_{C02}) with variable vapor contents, close to a fluid inclusions plan in the Qz3B. (H) Primary and pseudosecondary aqueous-carbonic three-phases fluid-inclusions (L_{H2O}-L_{CO2}-V_{C02}) contemporaneous with two-phases aqueous-carbonic fluid inclusions (L_{H2O}-L_{C02}), in the Qz3B. (I) and (J) Transmitted infrared-light photomicrographs of stibnite with primary two-phase aqueous inclusions (L_{H2O}-V_{H20}) along {110} or {010} growth planes, respectively.

Fig. 11. Microthermometric results of the different fluid-inclusions groups trapped in the quartz gangue, the scheelite, and the stibnite. (A) Distribution of the final ice melting temperatures (Tm ice) from the aqueous and aqueous-carbonic fluid inclusions. (B) Distribution of the final clathrate melting temperatures (Tm Clat) from the aqueous-carbonic fluid inclusions. (C) Distribution of the homogenization temperatures (Th) from the aqueous-carbonic fluid inclusions.

Fig. 12. (A) Evolution of the final ice melting temperatures (Tm ice) versus the homogenization temperatures (Th) diagram, of the aqueous and aqueous-carbonic fluid inclusions from the quartz gangue, the scheelite, and the stibnite. (B) Estimated P and T conditions from the

calculated isochores deduced form the FI study. The maximal regional metamorphism condition is after the estimations of Le Gall (1993).

Fig. 13. Sketch illustrating the paragenetic evolution associated to the deformation events and opening of the quartz-veins structure of the La Lucette deposit.

Fig. 14. (A) Synthesis of the structural control and radiometric age compilation of the Sb-Au and orogenic gold districts of the Armorican Massif including illite $^{40}Ar/^{39}Ar$ dating of the Semnon Sb-Au district (Pochon et al., 2018) and structural controls of the Quimper district (Fouquet, 1980), the Vendée district (Marcoux et al., 1984, Cheval-Garabédian, 2019, for Rochetréjoux and les Brouzils), la Bellière orogenic gold veins and Sb veins (Cheval-Garabédian et al., 2020a), Lopérec district (Bouchot et al., 1997). Abbreviations are the same as in figure 1. Geological map modified after Chantraine et al. (1996). (B) Structural interpretation of the La Lucette Sb-Au-(W) quartz-vein system emplacement as an "en echelon" tension gashes controlled by a dextral NW-SE striking shearing along the North Armorican Shear Zone. Modified from Serment (1978), after the mining plans of Bastit (1930). (C) Relative and absolute ages synthesis of the Sb-As, Sb-Au, orogenic-gold vein-type districts, and other mineralizing events through the European Variscan Belt. The district names for the Armorican Massif are reported in Figure 14A.

Fig. 15. Metallogenic model of the La Lucette Sb-Au-(W) deposit replaced in the Late-Variscan tectonic context of the North Armorican Shear Zone (NASZ).

Table 1 Summary of the microthermometric measures. Number of analyses (n), scheelite (Sch), stibnite (Sb). Melting temperature of solid CO_2 (Tm CO_2), homogenization temperature of CO_2 (Th CO_2), final melting temperature of ice (Tm ice), melting temperature of clathrate (Tm Cl), homogenization temperature (Th). All values are in °C. Typology of fluid-inclusions is explained in the text.

Table 2 Summary of the bulk composition data for representative three-phased aqueous-carbonic IF. The composition of the volatile phase was only deduced from the microthermometric measures.

Figures

Figure 1

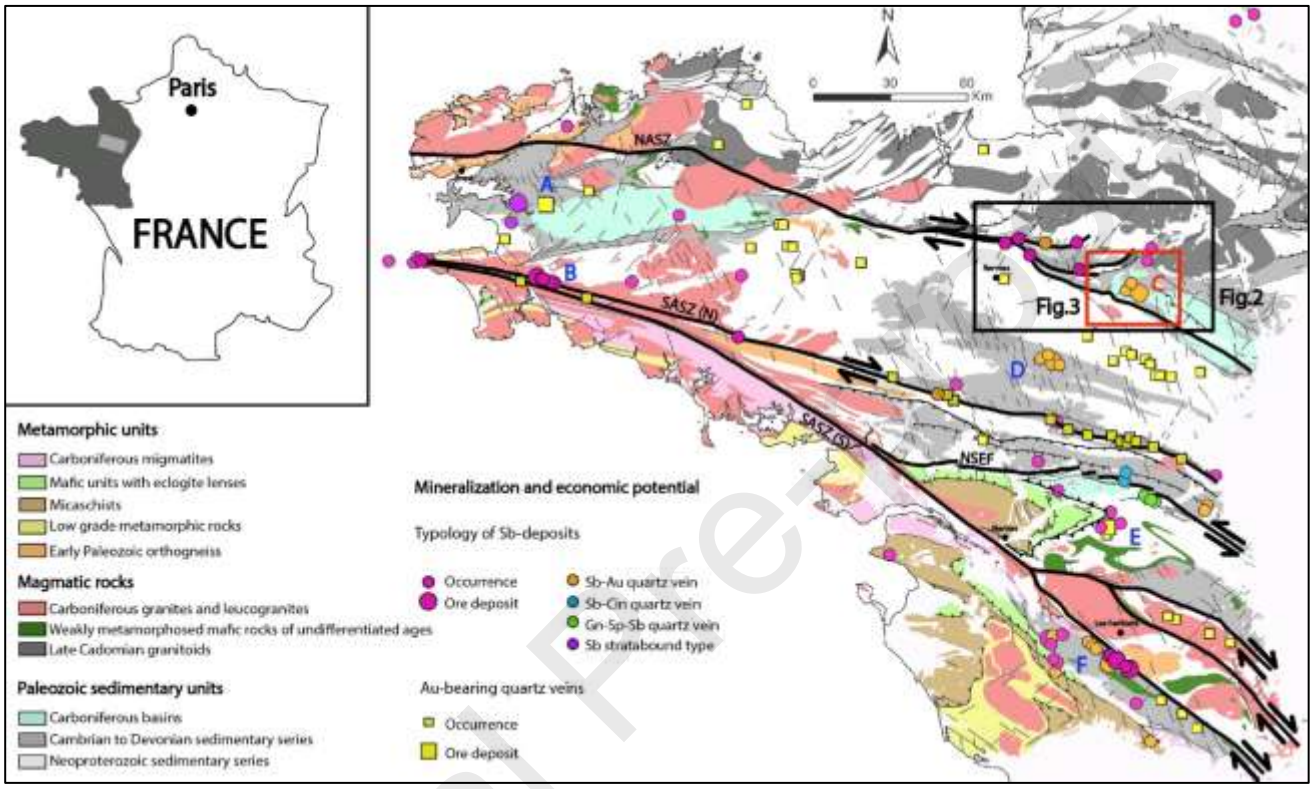

Figure 2

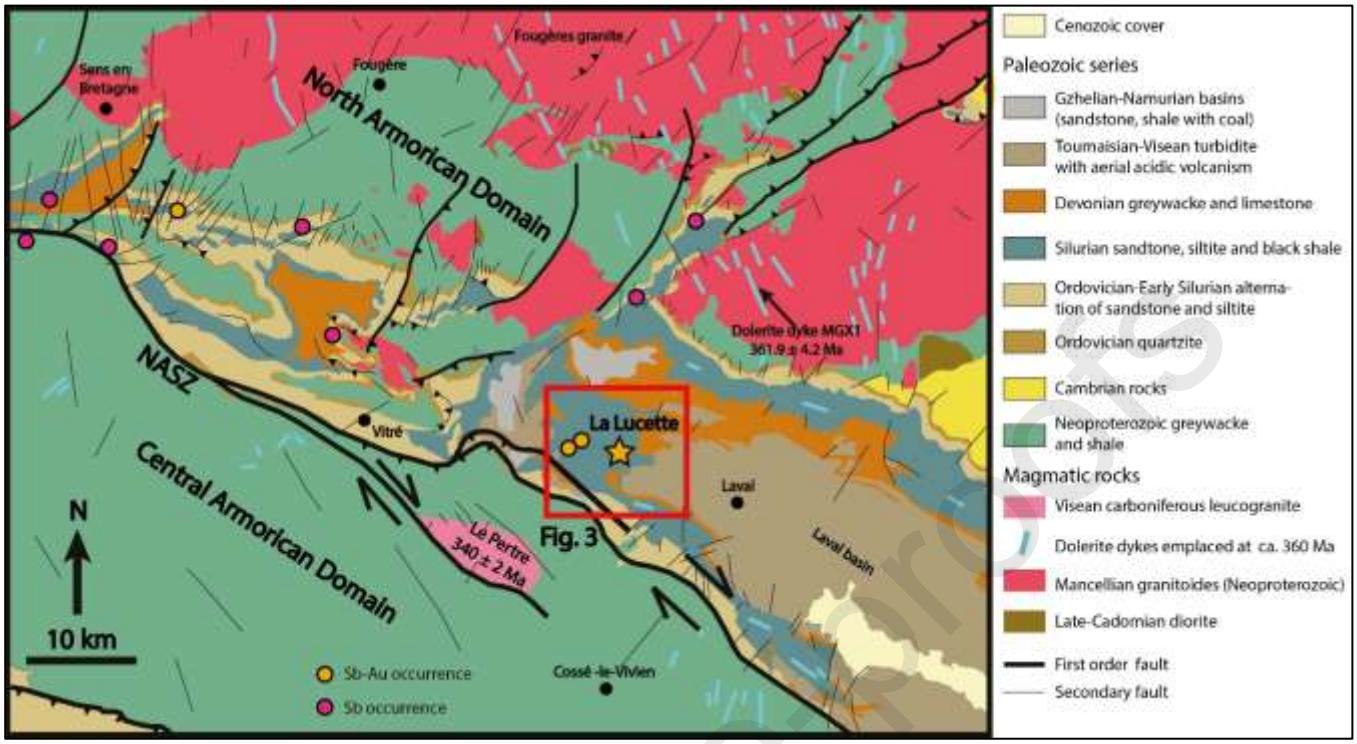

Figure 3

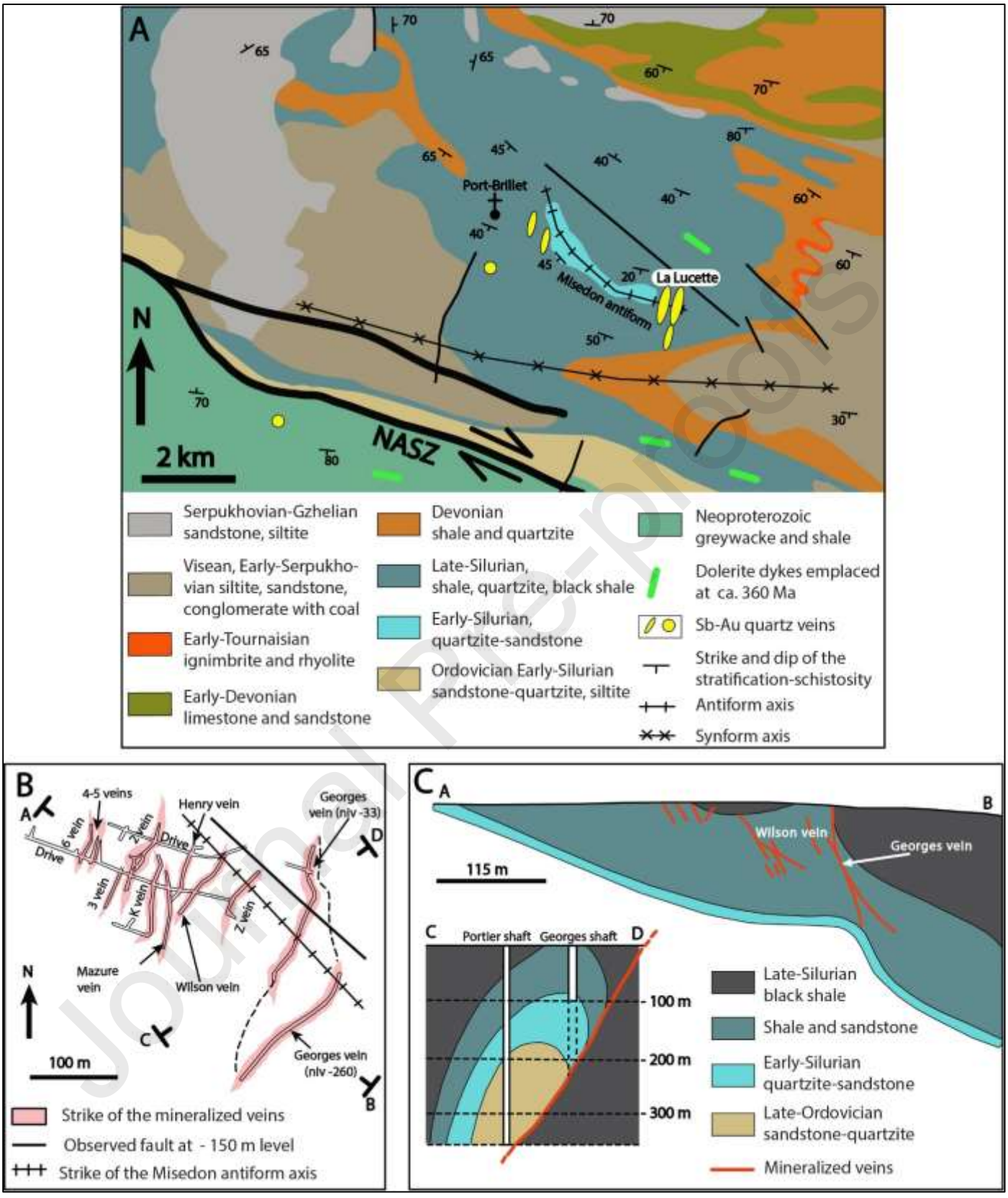
A
Port-Brillet
La Lucette
Misedon antiform
NASZ
N
2 km
Serpukhovian-Gzhelian sandstone, siltite
Visean, Early-Serpukhovian siltite, sandstone, conglomerate with coal
Early-Tournaisian ignimbrite and rhyolite
Early-Devonian limestone and sandstone
Devonian shale and quartzite
Late-Silurian, shale, quartzite, black shale
Early-Silurian, quartzite-sandstone
Ordovician Early-Silurian sandstone-quartzite, siltite
Neoproterozoic greywacke and shale
Dolerite dykes emplaced at ca. 360 Ma
Sb-Au quartz veins
Strike and dip of the stratification-schistosity
Antiform axis
Synform axis
B
4-5 veins
Henry vein
Georges vein (nlv -33)
Drive
6 vein
2 vein
3 vein
K vein
Z vein
Mazure vein
Wilson vein
Georges vein (nlv -260)
100 m
Strike of the mineralized veins
Observed fault at - 150 m level
Strike of the Misedon antiform axis
C
Wilson vein
Georges vein
115 m
Portier shaft
Georges shaft
100 m
200 m
300 m
Late-Silurian black shale
Shale and sandstone
Early-Silurian quartzite-sandstone
Late-Ordovician sandstone-quartzite
Mineralized veins

Figure 4

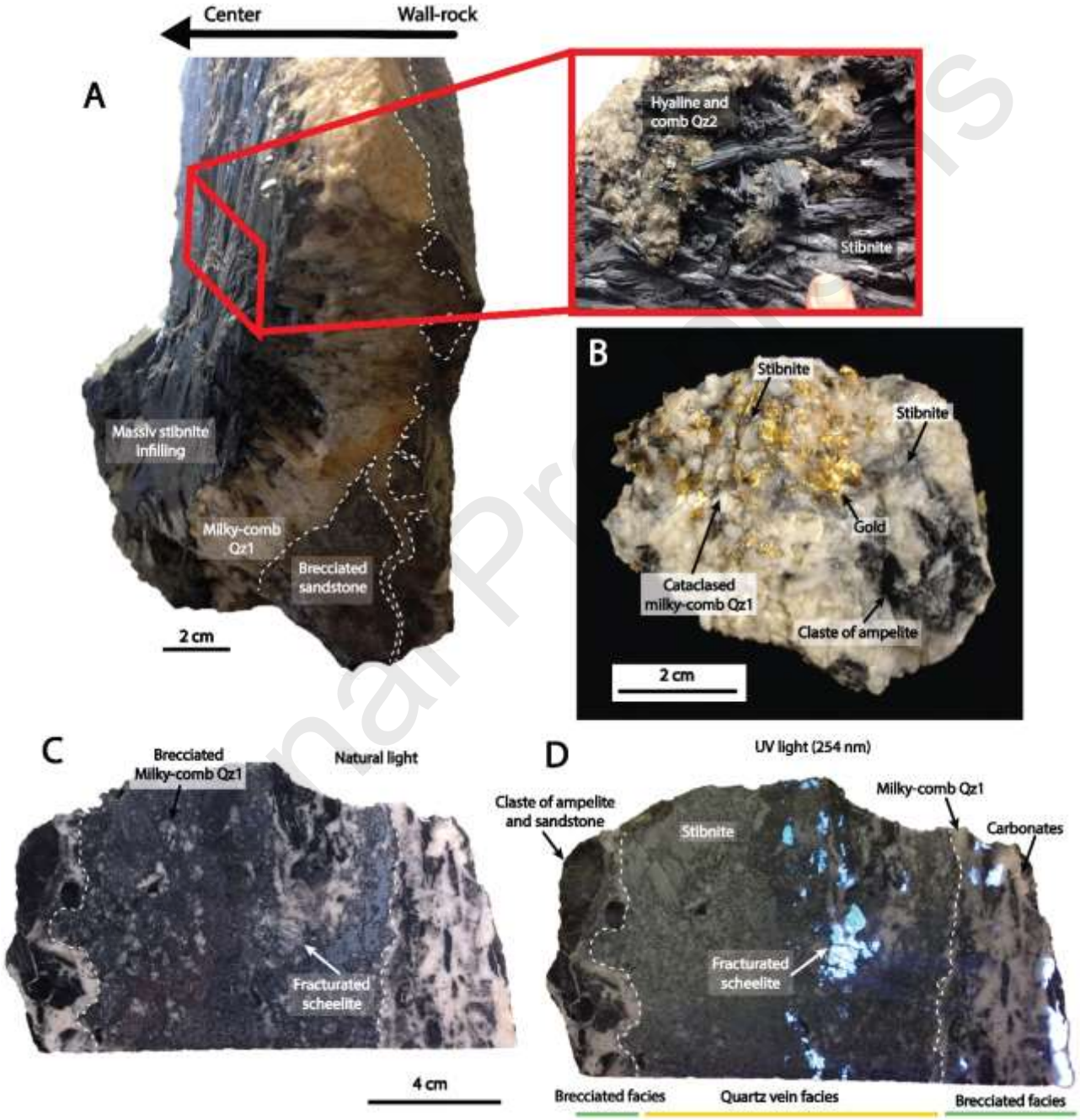
Center
Wall-rock
A
Hyaline and comb Qz2
Stibnite
Massiv stibnite infilling
Milky-comb Qz1
Brecciated sandstone
2 cm
B
Stibnite
Stibnite
Gold
Cataclased milky-comb Qz1
Claste of ampelite
2 cm
C
Brecciated Milky-comb Qz1
Natural light
Fracturated scheelite
4 cm
D
UV light (254 nm)
Claste of ampelite and sandstone
Stibnite
Milky-comb Qz1
Carbonates
Fracturated scheelite
Brecciated facies
Quartz vein facies
Brecciated facies

Figure 5

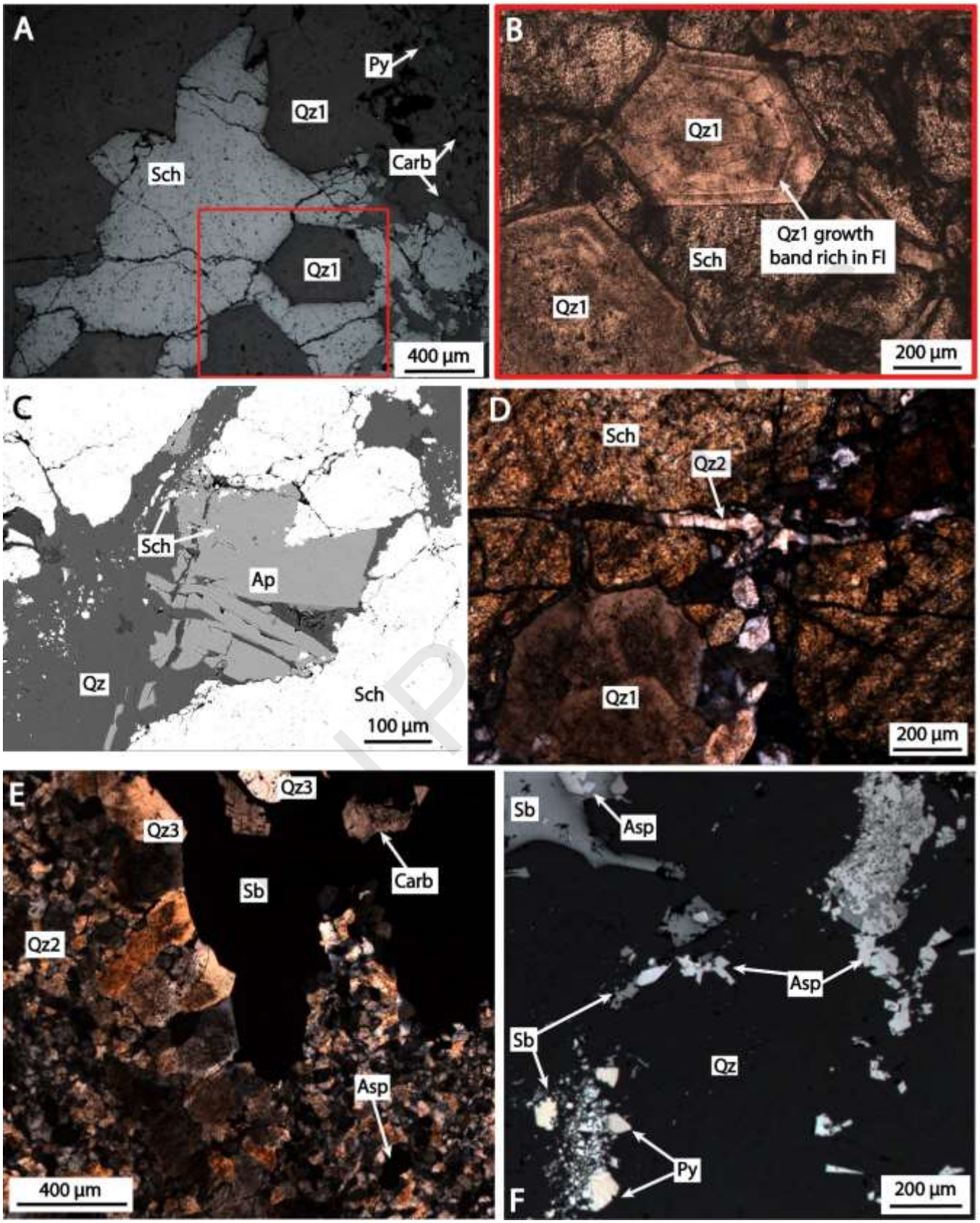
A
Py
Qz1
Carb
Sch
Qz1
400 µm
B
Qz1
Qz1 growth band rich in FI
Sch
Qz1
200 µm
C
Sch
Ap
Qz
Sch
100 µm
D
Sch
Qz2
Qz1
200 µm
E
Qz3
Qz3
Carb
Sb
Qz2
Asp
400 µm
Sb
Asp
Asp
Sb
Qz
Py
F
200 µm

Figure 6

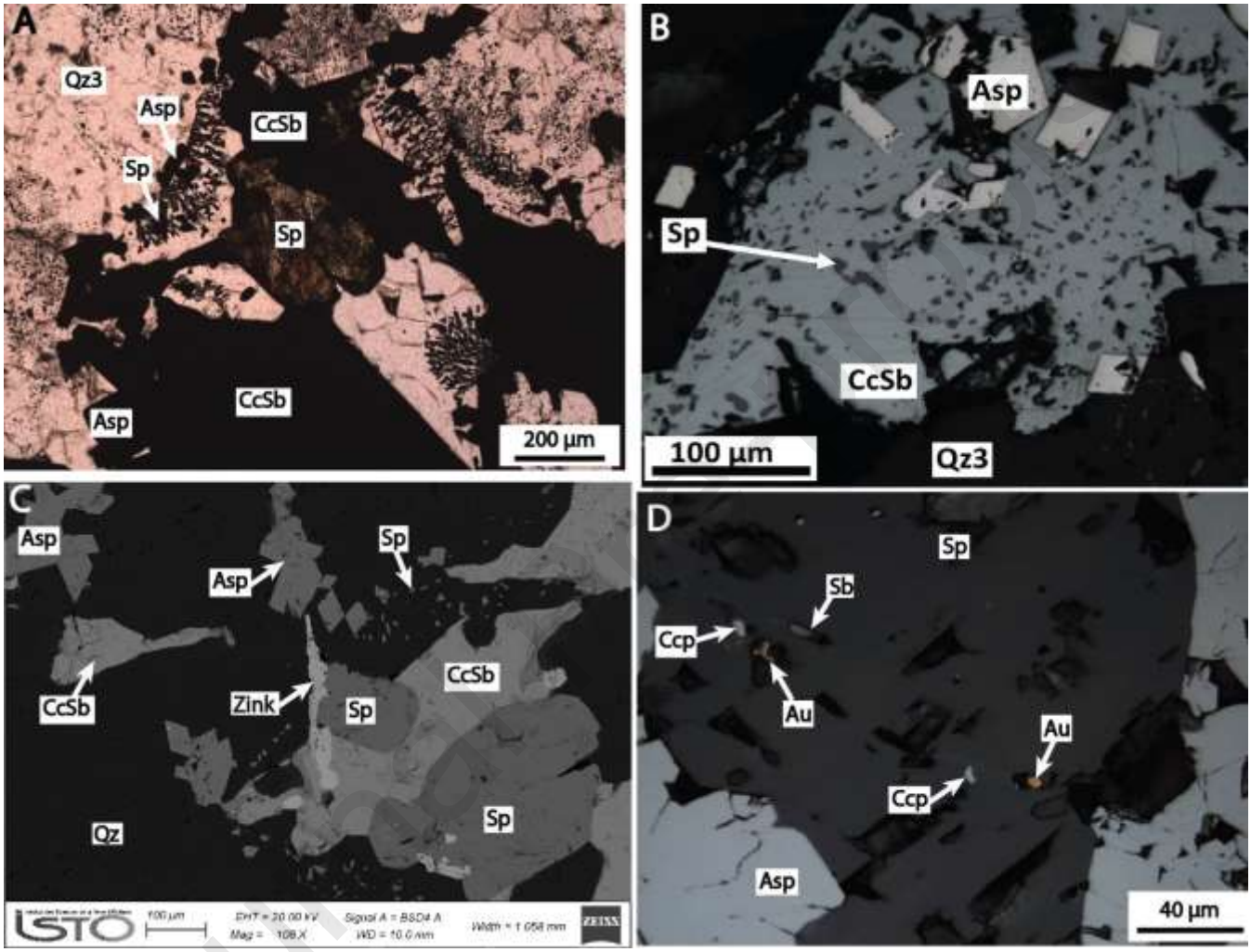

Figure 7

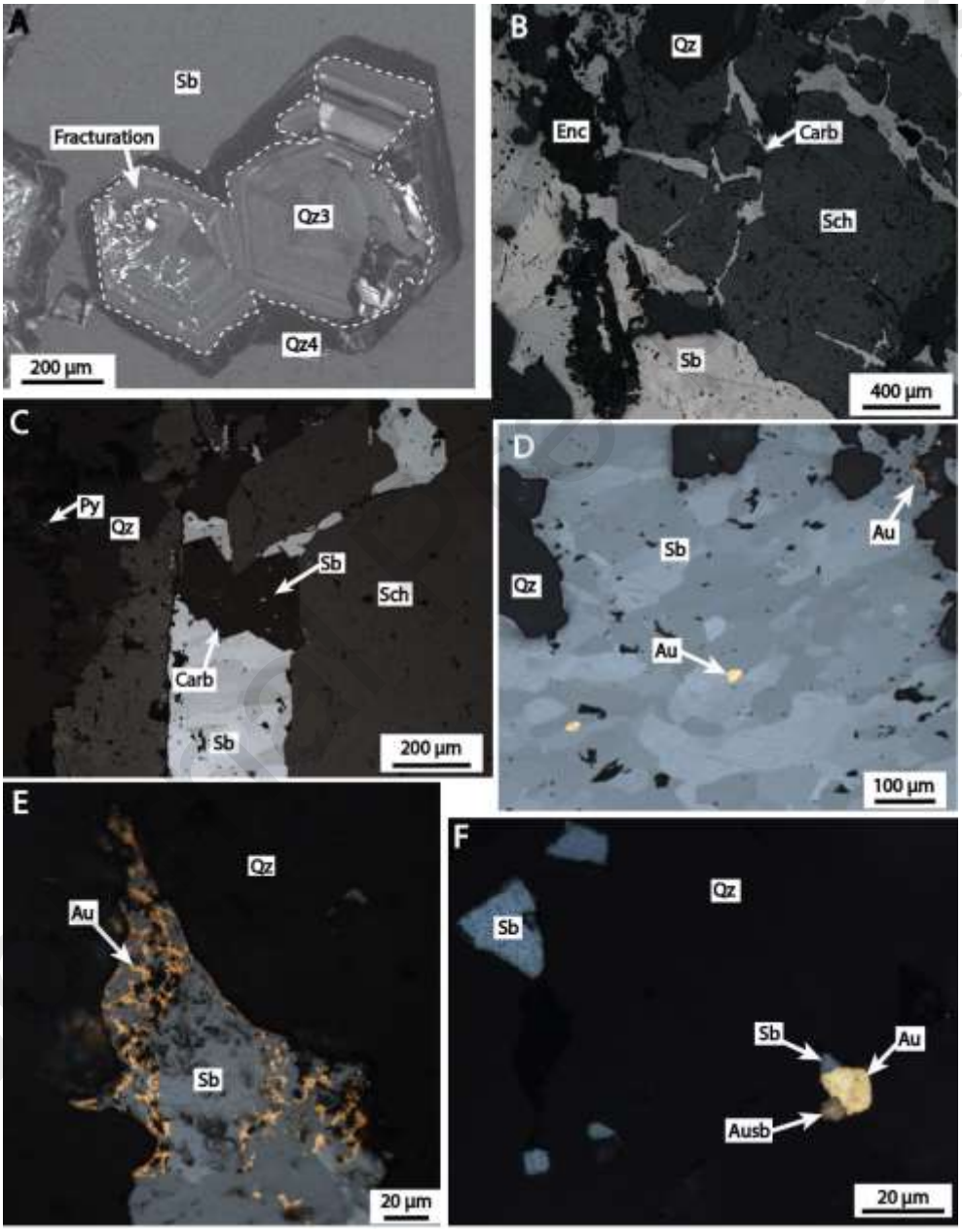
A
Sb
Fracturation
Qz3
Qz4
200 µm
B
Qz
Enc
Carb
Sch
Sb
400 µm
C
Py
Qz
Sb
Sch
Carb
Sb
200 µm
D
Sb
Au
Qz
Au
100 µm
E
Qz
Au
Sb
20 µm
F
Qz
Sb
Sb
Au
Ausb
20 µm

Figure 8

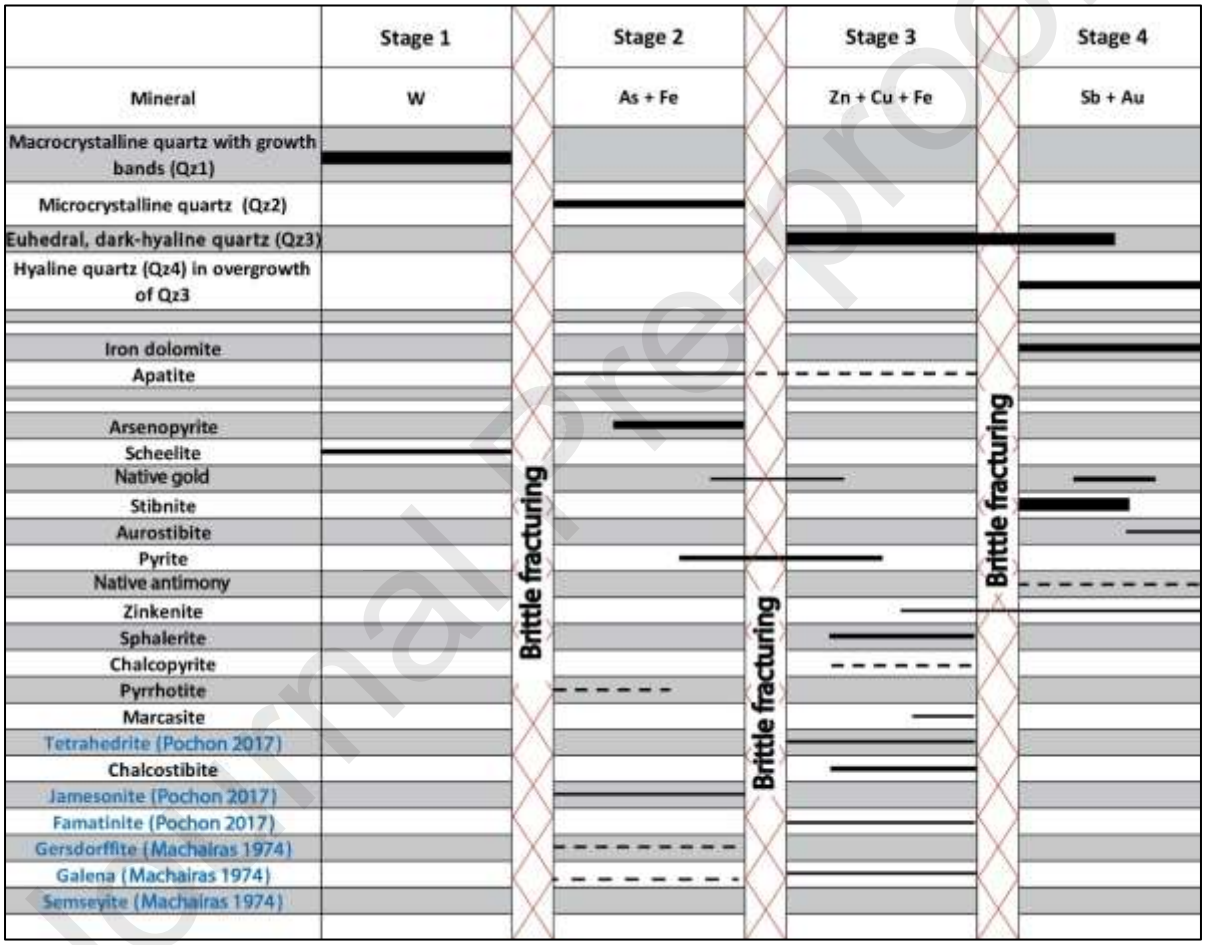

Figure 9

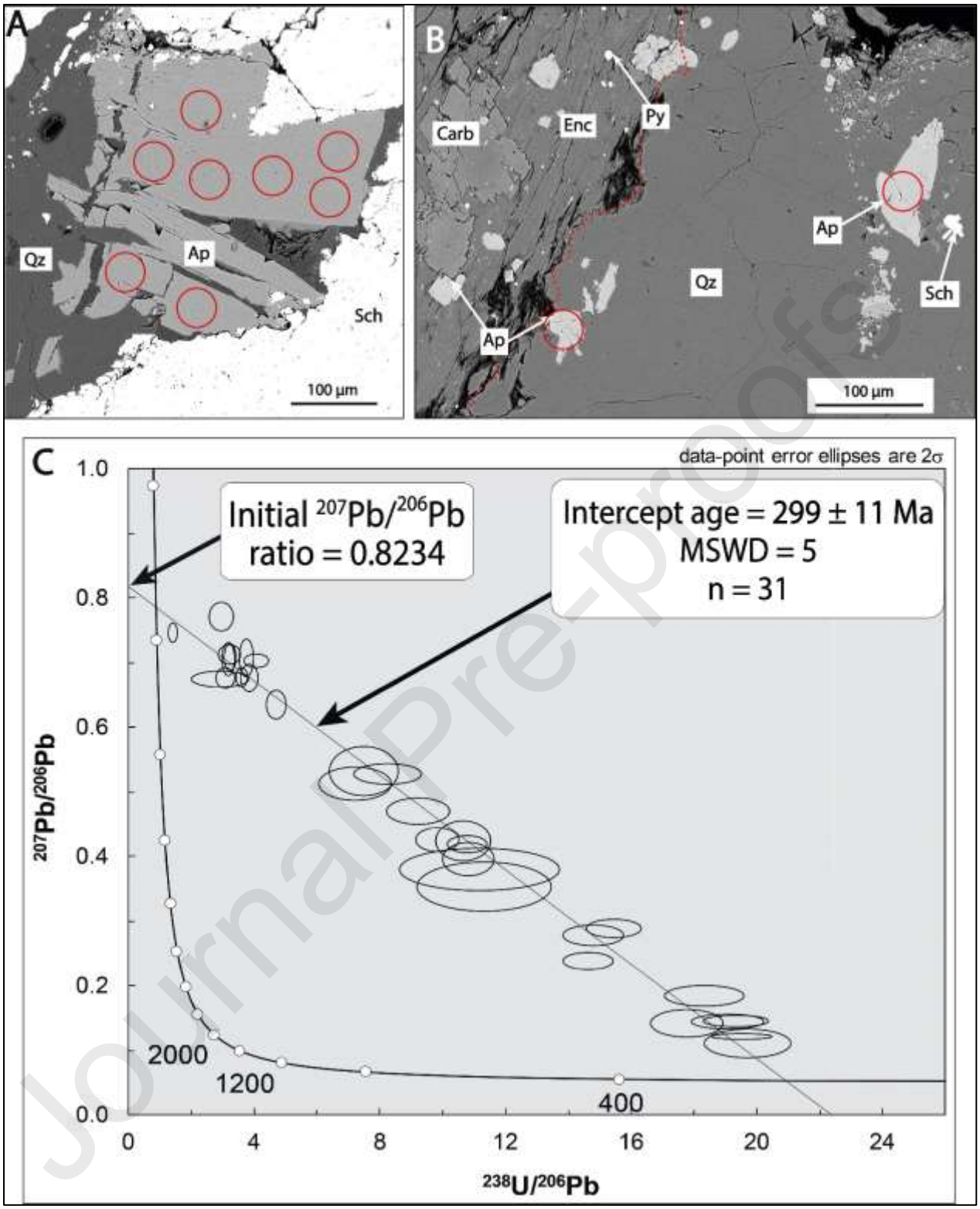

Figure 10

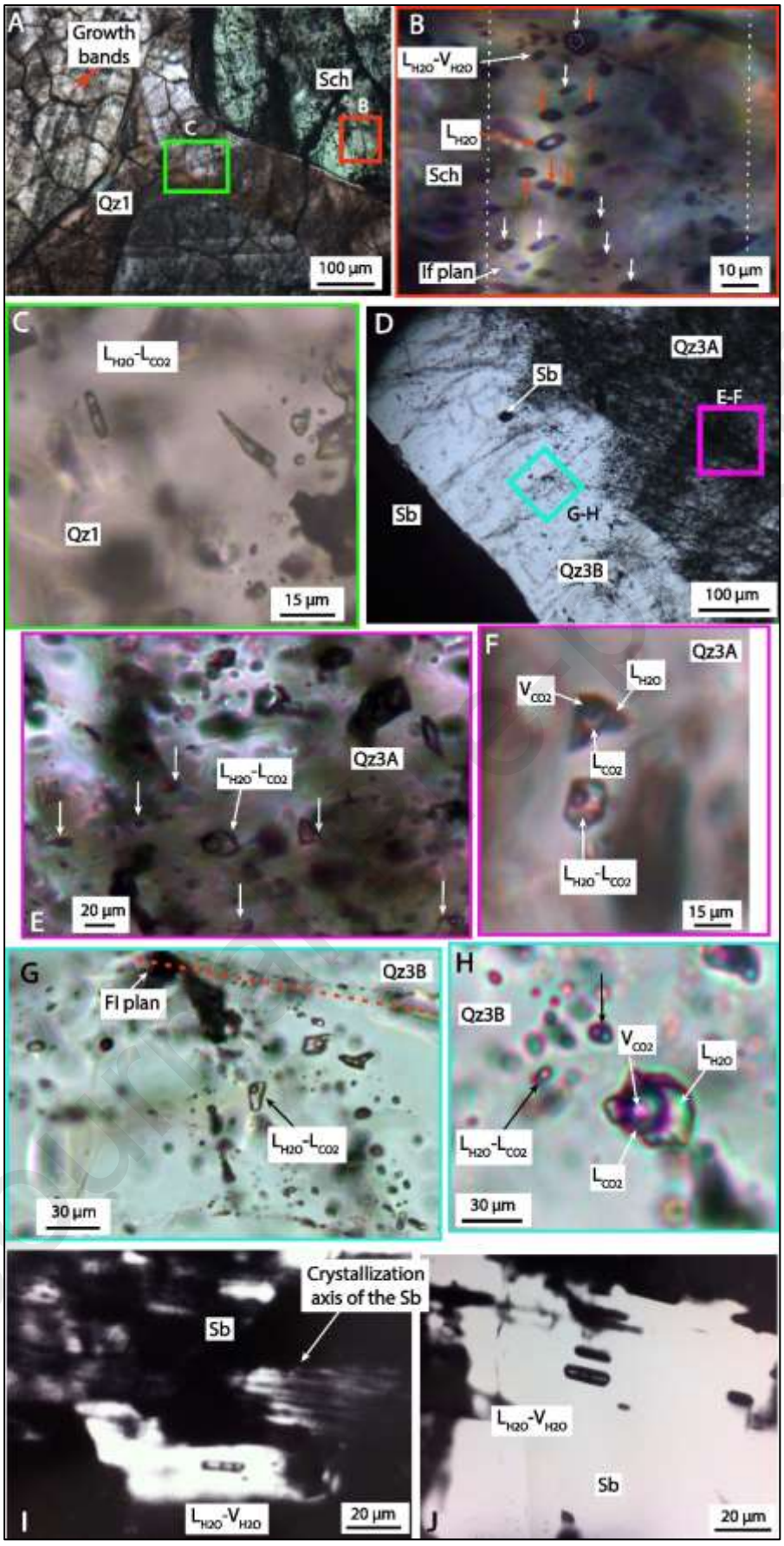
A
Growth bands
Sch
B
C
Qz1
100 µm
B
L_{H2O}-V_{H2O}
L_{H2O}
Sch
If plan
10 µm
C
L_{H2O}-L_{CO2}
Qz1
15 µm
D
Qz3A
Sb
E-F
G-H
Sb
Qz3B
100 µm
E
L_{H2O}-L_{CO2}
Qz3A
20 µm
F
Qz3A
V_{CO2}
L_{H2O}
L_{CO2}
L_{H2O}-L_{CO2}
15 µm
G
Qz3B
FI plan
L_{H2O}-L_{CO2}
30 µm
H
Qz3B
V_{CO2}
L_{H2O}
L_{H2O}-L_{CO2}
L_{CO2}
30 µm
Crystallization axis of the Sb
Sb
I
L_{H2O}-V_{H2O}
20 µm
L_{H2O}-V_{H2O}
Sb
J
20 µm

Figure 11

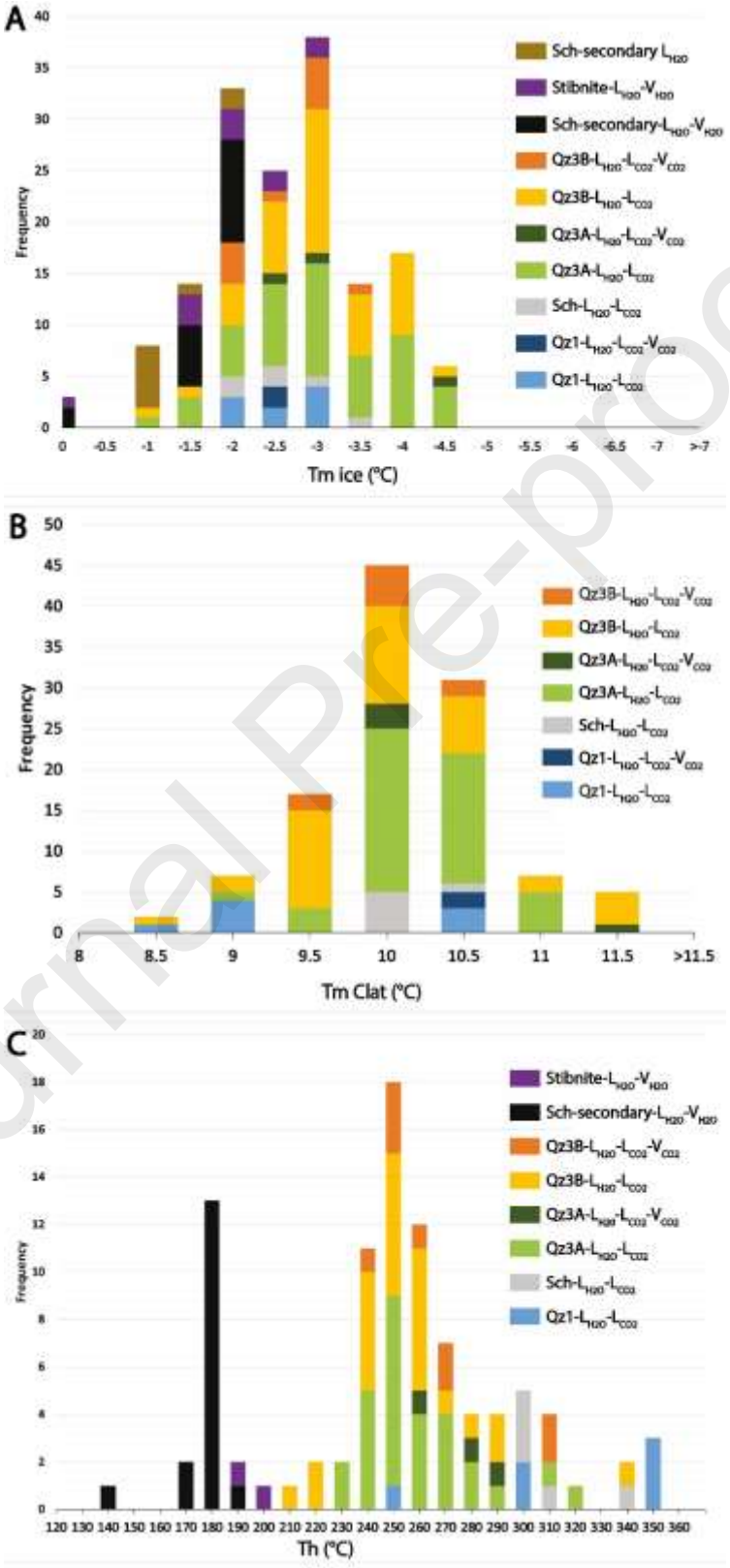

Figure 12

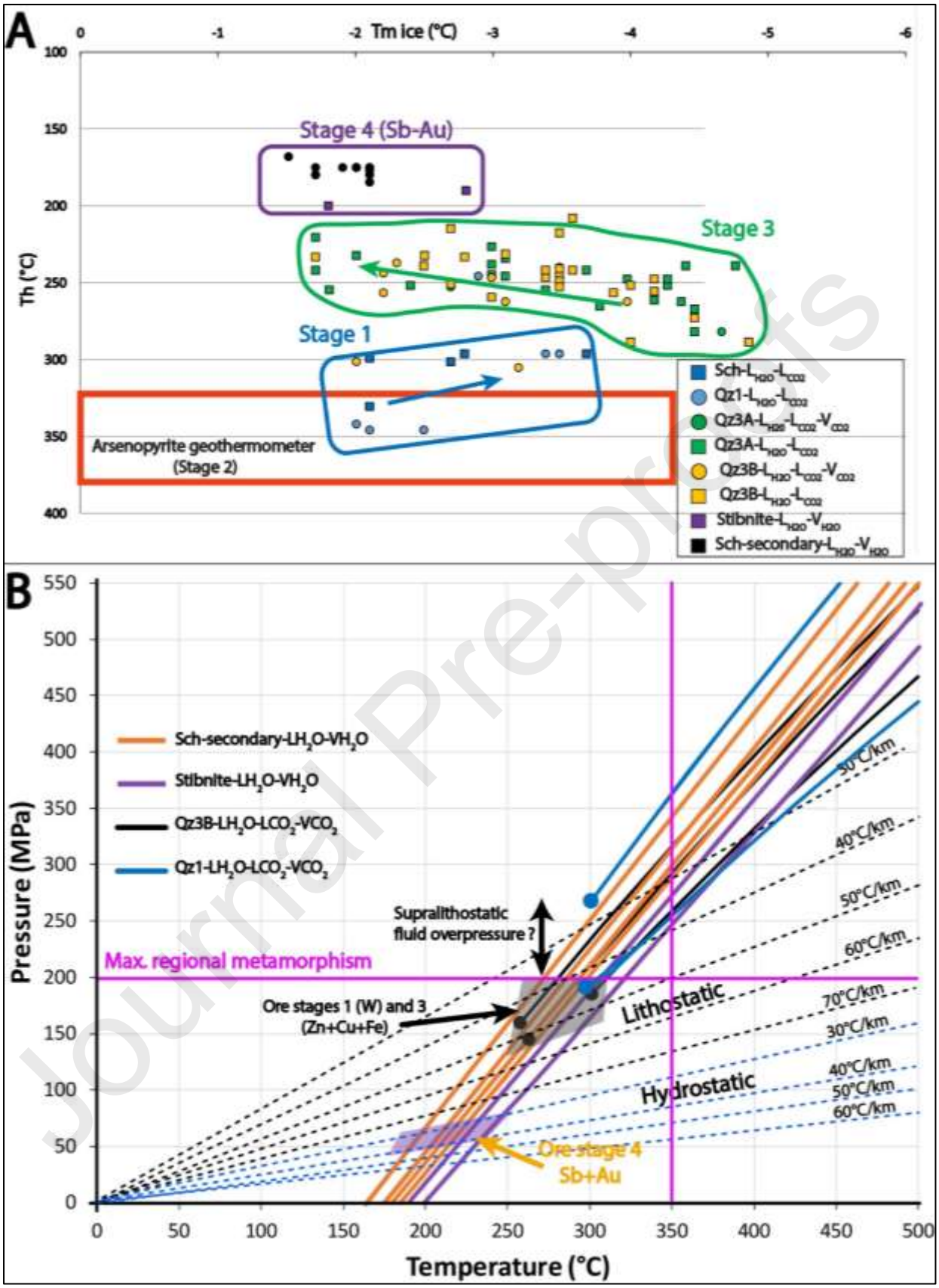

Figure 13

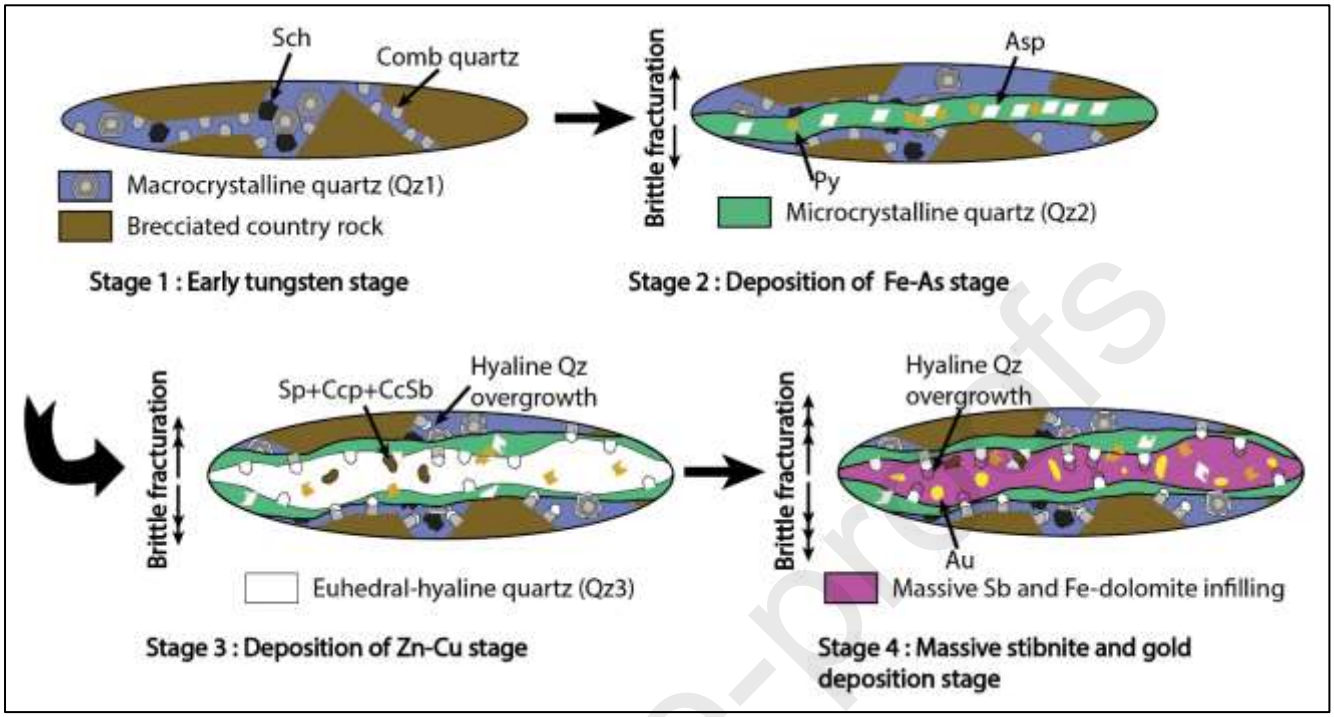

Figure 14

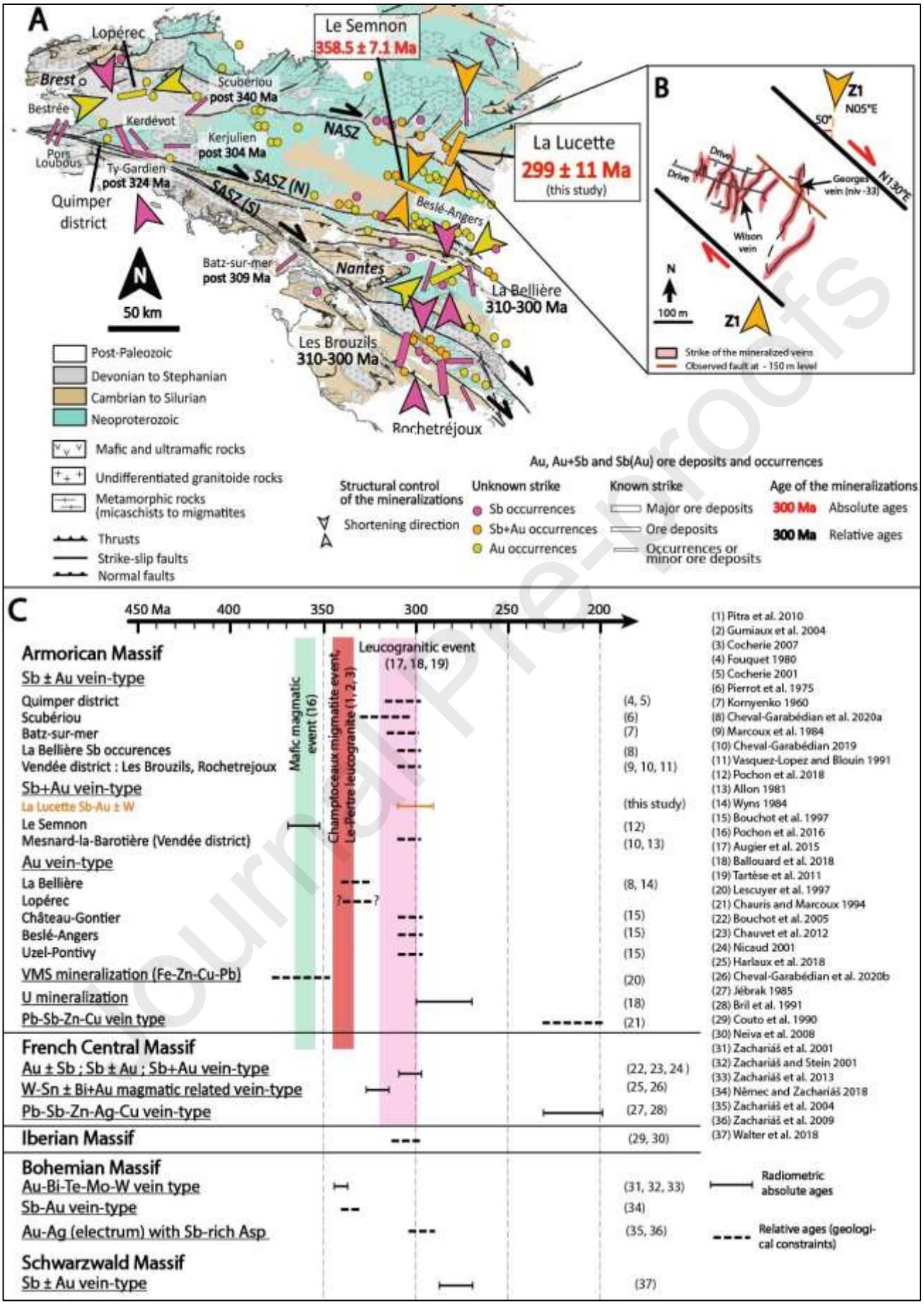

Figure 15

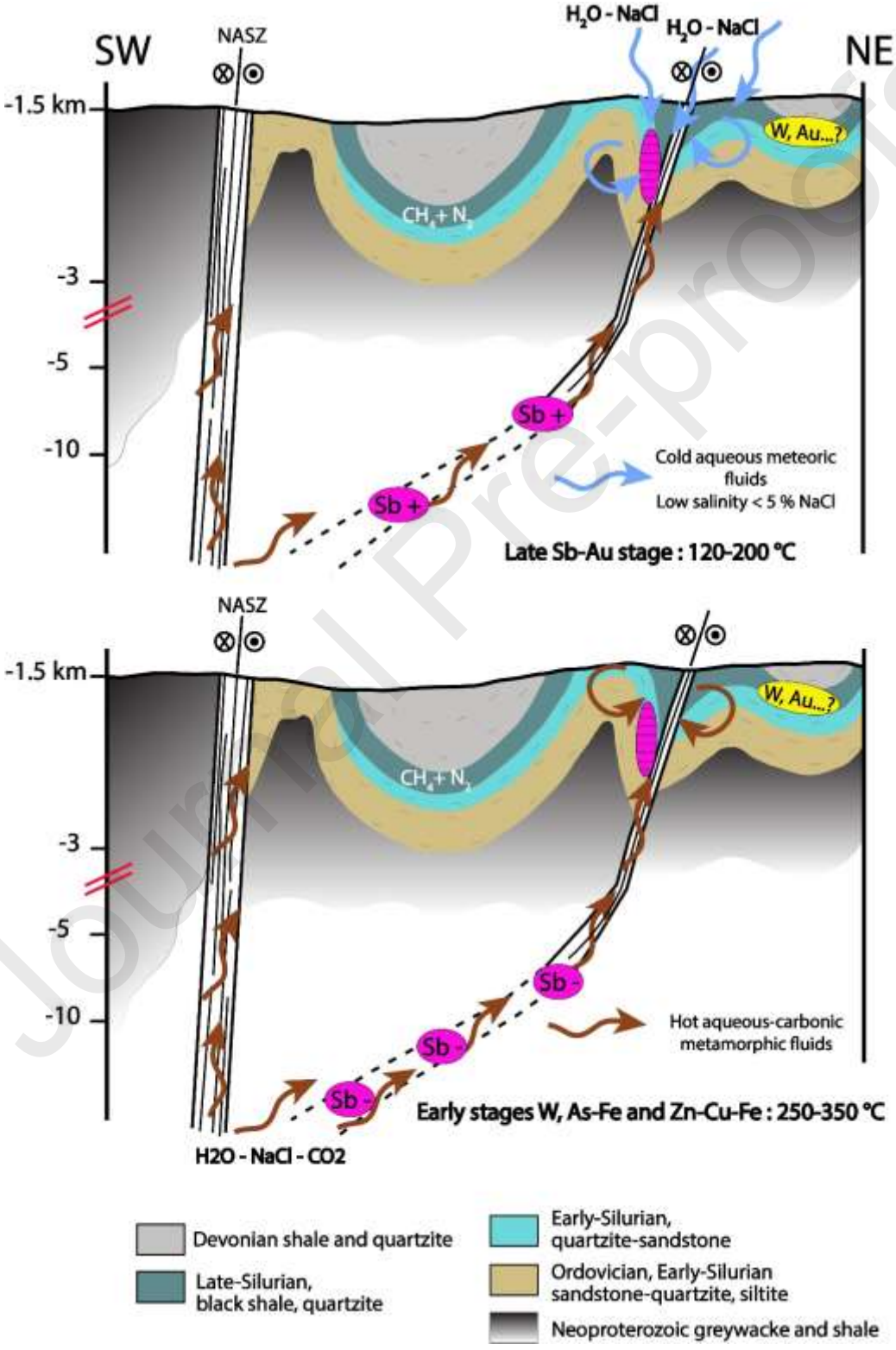

Tables

Table 1

Fluid inclusion types	Tm H_2O	Tm Cl	Th CO_2	Th
Sch-L_{H2O}-L_{CO2}	-2.8	9.8	-	305
n	6	6	-	5
Qz1-L_{H2O}-L_{CO2}-V_{CO2}	-2.7	10.3	21.9	-
n	2	2	2	-
Qz1-L_{H2O}-L_{CO2}	-2.9	9.9	-	312
n	9	6	-	6
Qz3A-L_{H2O}-L_{CO2}-V_{CO2}	-3.5	10.1	-	271
n	3	4	-	3
Qz3A-L_{H2O}-L_{CO2}	-3.5	10.2	-	253
n	50	48	-	27
Qz3B-L_{H2O}-L_{CO2}-V_{CO2}	-3.1	9.5	24.7	262
n	13	11	9	9
Qz3B-L_{H2O}-L_{CO2}	-3.4	9.8	-	249
n	39	41	-	24
Sch-secondary-L_{H2O}-V_{H2O}	-1.7	-	-	173
n	18	-	-	17
Sch-secondary-L_{H2O}	-1.5	-	-	-
n	9	-	-	-
Stibnite-L_{H2O}-V_{H2O}	-2.2	-	-	195
n	11	-	-	2

The temperatures of homogenization occur in the liquid phase for all FI.

Table 2

Sample	Ore stage	Fluid inclusion types	Degree of fill	Tm H_2O (°C)	Tm Cl	Th CO_2	Th	Bulk composition (mol %)		Salinity (wt. % NaCl)	Density (g/cm^3)
								H2O	CO2		
L5-1A	Stage 1	Qz1-L_{H2O}-L_{CO2}-V_{CO2}	0.73	-2.7	10.3	21.9	300	0.85	0.15	4.5	0.96
L5-1B	Stage 1	Qz1-L_{H2O}-L_{CO2}-V_{CO2}	0.55	-2.7	10.3	21.9	300	0.75	0.25	4.5	0.91
L8C-1A	Stage 3	Qz3B-L_{H2O}-L_{CO2}-V_{CO2}	0.62	-2	10.4	25.2	301	0.81	0.19	3.4	0.91
L8C-2B	Stage 3	Qz3B-L_{H2O}-L_{CO2}-V_{CO2}	0.65	-2.2	9.8	23.2	257	0.82	0.18	3.7	0.93
L8C-3	Stage 3	Qz3B-L_{H2O}-L_{CO2}-V_{CO2}	0.68	-4	9.7	25.8	262	0.82	0.18	6.5	0.94

300 = according to analyses from the Qz1-LH_2O-LCO_2 familly. Note that the temperatures of homogenization occur in the liquid phase for all FI.

Graphical abstract

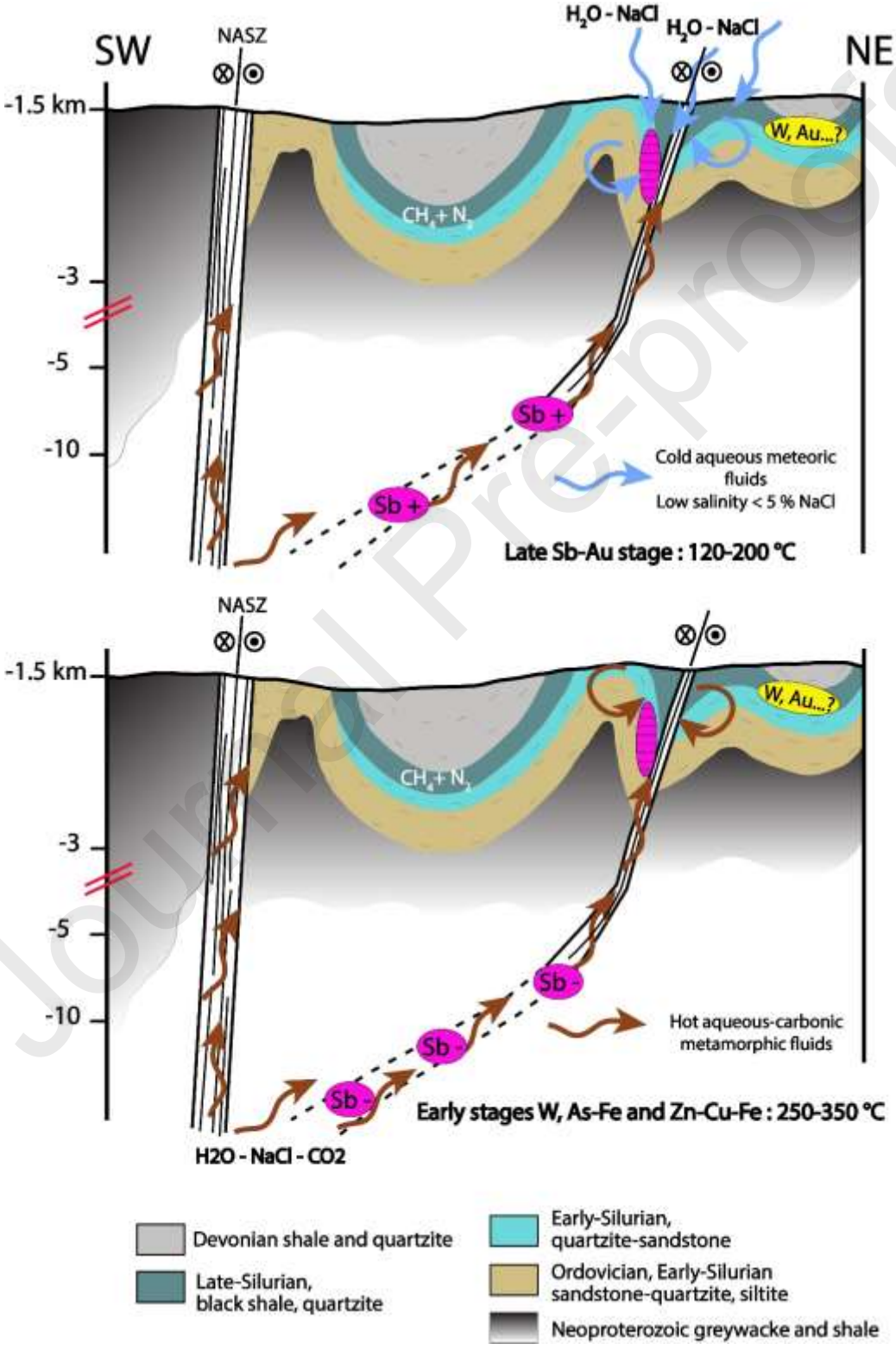

Declaration of interests

☐The authors declare that they have no known competing financial interests or personal relationships that could have appeared to influence the work reported in this paper.

☒The authors declare the following financial interests/personal relationships which may be considered as potential competing interests:

Florent cheval reports administrative support and equipment, drugs, or supplies were provided by Orleans Earth Sciences Institute. Florent Cheval reports a relationship with E-Mines that includes: employment.

Highlights:

- New metallogenic insights from la Lucette Sb-Au-(W) vein-deposit (Armorican Massif, France) to decipher the 310-295 Ma Sb-Au metallogenic peak in the European Variscan Belt.
- Shallow emplacement level (6 to 3.5 km) in a continuum of time, fluid mixing and cooling (~200 to 130°C), are key factors for the late Sb-Au ore-deposition.
- No additional magmatic source is needed for the ore genesis in the Armorican Massif, France.
- La Lucette Sb-Au-(W) ore-deposits corresponds to a different expression of the epizonal orogenic gold mineralization.